Draft version June 27, 2025
Typeset using LaTeX **twocolumn** style in AASTeX631

Thirty Two New Bright ZZ Ceti Stars from *TESS*: Adding Cycles 4 and 5

Alejandra D. Romero,[1] S. O. Kepler,[1] Gabriela Oliveira da Rosa,[1] and J. J. Hermes[2]

[1]*Instituto de Física, Universidade Federal do Rio Grande do Sul, 91501-970 Porto Alegre, RS, Brazil*
[2]*Department of Astronomy & Institute for Astrophysical Research, Boston University, 725 Commonwealth Ave., Boston, MA 02215, USA*

ABSTRACT

Analyzing all 120 s and 20 s light curves obtained by the TESS satellite up to Sector 69 — the end of the fifth year of observations — for all known white dwarfs and white dwarf candidates up to G=17.5 mag, we report the discovery of 32 new pulsating DA white dwarf stars. For all objects, we obtained the period spectra and performed a seismological analysis using full evolutionary models to estimate the structural parameters, such as effective temperature, stellar mass, and hydrogen envelope mass. The median stellar mass for the pulsators from asteroseismology is 0.609 $M_\odot$, in agreement with the median value of photometric and spectroscopic determinations, 0.602 $M_\odot$, excluding the low and extremely-low mass objects. Finally, we found rotational-splitting multiplets for 9 stars, which led to rotation periods between 4 h and 1 d.

Keywords: White dwarf stars - Surveys - Stellar oscillations

1. INTRODUCTION

The first variable white dwarf star was discovered by Arlo Landolt around 1960, when he was conducting photometric observations of faint standard stars at the Kitt Peak National Observatory. Landolt realized that one of the comparison stars, Haro–Luyten Taurus 76 or HL Tau 76, was actually variable itself, with a period of ~750 s (Landolt 1968). The second object was reported in 1971 by Lasker & Hesser (1971), who discovered photometric variability in the known DA white dwarf stars R548. Curiously, this object was already identified as a variable star and had been given the variable star name ZZ Ceti. R584 then became the prototype of the new class of pulsating white dwarfs known as ZZ Cetis (Van Horn 2015). By 2007, around 126 ZZ Cetis had been discovered (Kepler 2007). To date, approximately 500 ZZ Cetis have been confirmed (see for instance Bognar & Sodor 2016; Córsico et al. 2019; Romero et al. 2019b; Vincent et al. 2020; Guidry et al. 2021; Romero et al. 2022b).

Variable DA white dwarfs are found in a narrow range of effective temperature, between 10,000 K and 13,000 K, depending on stellar mass (Hermes et al. 2017; Kepler & Romero 2017). Pulsations are identified as nonradial gravity spheroidal modes with low harmonic degrees, with variation periods ranging from 70 to 2000 seconds and amplitudes up to 0.3 magnitudes (Bognar & Sodor 2016). Pulsations are driven by an excitation mechanism known as the κ-γ mechanism, related to an opacity bump due to partial hydrogen ionization at the base of the hydrogen-rich envelope (Dolez & Vauclair 1981; Winget et al. 1982). As the star cools, the outer convection layer thickens and the convective driving mechanism begins to dominate (Brickhill 1991; Goldreich & Wu 1999).

ZZ Ceti stars can be classified into three categories: hot, intermediate, and cool, based on their effective temperature and pulsational properties (Clemens 1993; Mukadam et al. 2006). Hot ZZ Cetis are found at the blue edge of the instability strip and exhibit stable light curves with short periods (less than 350 seconds) and small amplitudes (1.5 to 20 millimagnitudes). Cool ZZ Cetis, on the other hand, are situated at the red edge of the instability strip. They show long periods (up to 1500 s) with larger variation amplitudes (40 to 110 millimagnitudes) and nonsinusoidal light curves characterized by mode interference. Intermediate ZZ Cetis share the characteristics of both hot and cold members. Usually, for periods longer than 800 s, numerous peaks are detected in the Fourier transform, under a broad envelope that can be related to stochastically driven oscillations (Montgomery et al. 2020). Finally, the number of detected periods seems to increase at lower effective temperatures.

The Transiting Exoplanet Survey Satellite (TESS) was launched on April 18, 2018, its primary mission being to search for exoplanets around bright stars with the transit method (Ricker et al. 2014). During the first five cycles, the TESS mission has contributed significantly to the study of stellar pulsations in compact objects, in particular for hydrogen-rich atmosphere DA white dwarfs, through continuous and stable photometry, as well as its wide sky coverage (Bognár et al. 2020; Wang et al. 2020; Romero et al. 2022b; Bognár et al. 2023). During the first two cycles,

120-second cadence observations were available for selected targets, while for the extended mission for 2020-2022 many objects were observed at 20-second cadence, providing the opportunity to resolve the shortest pulsation periods of hot ZZ Ceti stars. The activities related to compact pulsators are coordinated by the Evolved Compact Stars with TESS Working Group (WG8) of the TESS Asteroseismic Science Consortium.

Romero et al. (2022b) presented the discovery of 74 new ZZ Cetis based on TESS data from the first three cycles, from Sectors 1 to 39, including data from 120 s and 20 s cadence. They complemented the space-based data with ground-based observations for 11 objects, leading to the discovery of an additional ZZ Ceti, TIC 20979953, which was part of the target list for the TESS mission, but no data had been taken. Romero et al. (2022b) also detected multiplets for four objects in the sample, leading to rotation periods from one to a few hours. In this paper, we continue their work by including in our analysis the data taken by the TESS mission during its fourth and fifth years, from Sectors 40 to 69 with 120 s- and 20 s-cadence. As a result, we present the discovery of 32 new ZZ Cetis. In addition, we present an updated period list for 21 objects reported by Romero et al. (2022b).

This paper is organized as follows. We present the sample of the 53 ZZ Cetis analyzed in this work, including the 32 new pulsating DA white dwarfs, in Section 2. We describe sample selection and data reduction for the TESS data in Section 3. In Section 4 we present the detected pulsation periods and perform an asteroseismological study for our sample in Section 5. In Section 6 we present a study of the sample of 103 pulsating DA white dwarfs discovered using data from the first five years of the *TESS* mission. We conclude in Section 7 by summarizing our findings.

2. NEW ZZ CETI STARS

As a continuation of the work of Romero et al. (2022b), we analyse the data from the fourth and fifth cycles of TESS, corresponding to Sectors 40 to 69, including data from 120 s and 20 s cadence. We look for newly observed ZZ Ceti stars, as well as for new data for objects that were already visited in previous cycles. As a result, we report 32 new ZZ Ceti stars, 12 new ZZ Cetis confirmed as pulsators with newly added data, and 20 objects observed only during the fourth and fifth cycles. Finally, 21 ZZ Cetis reported as variables in Romero et al. (2022b) were also observed in Sectors 40 to 69, and for those we update their period list. All targets analyzed are listed in Table 1, where we include the coordinates in J2000, the G magnitude, the effective temperature, surface gravity, and stellar mass. The last column indicates whether the object was reported as a ZZ Ceti by Romero et al. (2022b) (R22), or was confirmed as a pulsating DA white dwarf after observations from Sectors 40 to 69 were obtained (new).

The values for surface gravity and effective temperature listed in Table 1 were taken from various works, which used different techniques to determine atmospheric parameters (see the references in column 8). Most of the data is taken from Gentile Fusillo et al. (2019, 2021), and were determined using the magnitudes of *Gaia* DR2 and DR3 and parallax, combined with hydrogen models from Tremblay et al. (2011).

Photometric determinations of atmospheric parameters were also taken from the works of Kilic et al. (2020) and Vincent et al. (2020). The authors used parallaxes from *Gaia* DR2 and photometry from the Sloan Digital Sky Survey (Eisenstein et al. 2006; Kleinman et al. 2013; Kepler et al. 2019) and the Panoramic Survey Telescope and Rapid Response System (Chambers et al. 2016). They used pure hydrogen atmosphere models from Bergeron et al. (2019), applying the photometric technique described in Bergeron et al. (1997). Spectroscopic determinations of the effective temperature and surface gravity were taken from Gianninas et al. (2011); Limoges et al. (2013); Raddi et al. (2017); Kepler et al. (2019) and Tremblay et al. (2020). The stellar mass values were estimated by linear interpolation of evolutionary tracks in the cooling sequences described in Romero et al. (2019b) in the $\log g - T_{\rm eff}$ plane, given the values of surface gravity and effective temperature from Table 1.

We show the location of all the objects listed in Table 1 in the $T_{\rm eff} - \log g$ plane in Figure 1 (black circles). For targets that have more than one determination of atmospheric parameters, we consider the determination from Gentile Fusillo et al. (2021). We also include in Figure 1 the ZZ Ceti stars extracted from the works of Bognar & Sodor (2016); Hermes et al. (2017); Su et al. (2017); Romero et al. (2019a); Vincent et al. (2020); Romero et al. (2022b) (purple squares). All effective temperature and surface gravity values derived from spectroscopy were corrected by 3D convection (Tremblay et al. 2013; Córsico et al. 2019). As expected, most targets have masses close to the mean mass of white dwarfs ~ 0.6 M$_\odot$ (e.g. Kepler et al. 2021; O'Brien et al. 2023). In our analyzed sample, there are five objects with stellar masses in the range of $0.30 \leq M_*/M_\odot \leq 0.45$, which correspond to low-mass white dwarfs (Kilic et al. 2007; Istrate et al. 2016; Pelisoli & Vos 2019) and can harbor either a He/C/O core or a He core, depending on the evolution of the progenitor star (Romero et al. 2022a). Also, one object, TIC 0264172524, has a photometric mass of ~ 0.25 M$_\odot$ likely an extremely low-mass (ELM) white dwarf variable.

Table 1. List of the 53 ZZ Ceti observed by TESS presented in this work. Column 1 indicates the TIC identifier. The sexagesimal right ascension (RA) and declination (DEC) in J2000 are listed in columns 3 and 4, and the G magnitude is listed in column 5. The effective temperature, $\log g$ and stellar mass determinations are listed in columns 6, 7 and 8, respectively. Column 9 indicates the reference for the atmospheric parameters. Data were taken from the works of (a) Kilic et al. (2020) (b) Gentile Fusillo et al. (2021), (c) Tremblay et al. (2020) (d) Gentile Fusillo et al. (2019), (e) Montreal White Dwarf Database (Dufour et al. 2017) (f) Limoges et al. (2013) (g) Vincent et al. (2020) (h) S22 (i) Kepler et al. (2019), (j) Gianninas et al. (2011), (k) Raddi et al. (2017) and (l) Kawka & Vennes (2012). The last column indicates whether the object was discovered as a ZZ Ceti by Romero et al. (2022b) (R22), or if it was confirmed as a pulsating DA white dwarf in this work (new).

TIC	RA	DEC	G	$T_{\rm eff}$ [K]	$\log g$	Mass [$M_\odot$]	Ref.	
0001116746	10:23:00.51	+24:07:04.5	16.44	11608 ± 82	8.014 ± 0.013	0.612 ± 0.007	a	new
···	···	···	···	12127 ± 320	8.043 ± 0.041	0.629 ± 0.022	b	···
0007675859	18:12:22.74	+43:21:07.6	16.24	12445 ± 142	8.49 ± 0.009	0.900 ± 0.005	a	R22
···	···	···	···	12240 ± 214	8.479 ± 0.023	0.893 ± 0.014	b	···
0014448610	07:23:00.20	+16:17:04.4	15.08	11760 ± 80	8.29 ± 0.02	0.777 ± 0.012	c	new
0021187072	18:26:06.04	+48:29:11.3	16.28	11808 ± 228	7.235 ± 0.025	0.320 ± 0.006	b	R22
0030545382	13:16:30.82	−39:24:04.8	15.77	12093 ± 233	7.221 ± 0.028	0.3177 ± 0.007	b	new
0033717565	04:05:36.39	−76:28:28.1	16.50	10675 ± 172	7.639 ± 0.031	0.447 ± 0.012	b	R22
0055650407	04:55:27.27	−62:58:44.6	14.97	11838 ± 150	7.945 ± 0.019	0.576 ± 0.009	b	R22
0063281499	22:28:58.15	−31:05:53.7	15.61	12200 ± 220	8.02 ± 0.06	0.616 ± 0.032	k	R22
···	···	···	···	11712 ± 166	7.981 ± 0.025	0.594 ± 0.013	b	···
0072517198	13:49:03.63	+14:19:54.9	16.64	10750 ± 350	7.75 ± 0.038	0.493 ± 0.022	e	new
0079353860	21:18:15.52	−53:13:22.7	15.92	11123 ± 44	7.944 ± 0.004	0.571 ± 0.002	d	R22
0081848974	11:12:21.43	−51:30:03.9	16.40	11033 ± 191	7.977 ± 0.035	0.590 ± 0.018	b	new
0088046487	09:50:06.95	+18:37:33.9	16.68	11576 ± 298	7.978 ± 0.050	0.592 ± 0.026	b	new
0094748632	07:31:45.12	+23:53:53.0	16.14	11779 ± 222	8.025 ± 0.032	0.618 ± 0.017	b	new
0103700861	10:23:12.65	+67:25:06.5	16.80	8477 ± 103	8.060 ± 0.033	0.630 ± 0.018	b	new
0114058447	03:41:10.53	+19:08:00.4	15.84	9304 ± 106	7.533 ± 0.030	0.397 ± 0.011	b	new
0141179495	12:01:09.51	+42:59:47.4	16.11	11882 ± 179	8.018 ± 0.026	0.615 ± 0.014	b	new
0149863849	17:43:49.28	−39:08:25.9	13.53	11604 ± 206	8.087 ± 0.027	0.652 ± 0.015	b	R22
0159973152	03:20:31.41	−36:56:57.6	16.50	10715 ± 193	7.893 ± 0.042	0.546 ± 0.021	b	new
0192937035	08:08:56.78	+46:13:00.1	16.23	11542 ± 260	7.398 ± 0.031	0.363 ± 0.008	b	new
0201860926	02:31:56.01	−53:57:53.2	16.78	11353 ± 244	7.895 ± 0.042	0.548 ± 0.021	b	new
0230384389	19:03:19.56	+60:35:52.6	15.01	11550 ± 178	8.07 ± 0.05	0.642 ± 0.027	f	R22
···	···	···	···	10858 ± 63	···	0.624 ± 0.006	g	···
0261400271	06:18:13.07	−80:11:55.2	14.90	12731 ± 762	8.36 ± 0.04	0.819 ± 0.024	h	R22
0264172524	19:38:19.58	+69:09:11.3	16.42	13867 ± 467	6.935 ± 0.047	0.254 ± 0.006	b	new
0273206673	04:33:50.99	+48:50:39.1	15.86	11433 ± 221	7.966 ± 0.035	0.586 ± 0.018	b	R22
0304024058	09:22:56.24	−68:16:48.7	16.10	11368 ± 208	7.955 ± 0.033	0.580 ± 0.017	b	R22
0317153172	23:22:31.91	−83:13:13.3	16.47	11813 ± 314	8.032 ± 0.042	0.622 ± 0.022	b	R22
0317620456	18:43:35.47	+27:40:26.8	16.92	10566 ± 57	···	0.603 ± 0.006	g	R22
0343296348	17:43:44.00	−74:24:37.5	15.85	11597 ± 150	7.968 ± 0.023	0.587 ± 0.011	b	R22
0353727306	02:40:29.66	+66:36:37.0	15.60	11554 ± 171	8.020 ± 0.025	0.615 ± 0.013	b	R22

Table 1 *continued*

Table 1 *(continued)*

TIC	RA	DEC	G	$T_{\rm eff}$ [K]	log g	Mass [$M_\odot$]	Ref.	
0375199799	20:37:50.60	+06:12:27.6	16.41	11310 ± 203	8.007 ± 0.036	0.607 ± 0.019	b	new
0409732714	08:24:03.35	−12:19:43.6	14.74	12176 ± 154	7.874 ± 0.016	0.540 ± 0.007	b	new
0423658036	13:29:24.81	−23:52:16.7	16.01	13910 ± 459	8.02 ± 0.06	0.620 ± 0.031	j	new
...	...	...	...	13650 ± 219	8.002 ± 0.024	0.610 ± 0.012	b	...
0453210132	07:51:41.50	+11:20:29.8	16.41	11791 ± 62	7.923 ± 0.009	0.564 ± 0.005	a	new
...	...	...	...	11818 ± 175	7.917 ± 0.028	0.561 ± 0.014	b	...
0461203226	12:06:50.89	−38:05:49.2	15.67	11866 ± 153	8.073 ± 0.021	0.645 ± 0.011	b	new
0600589802	01:00:25.56	+42:18:40.9	16.56	11377 ± 256	7.992 ± 0.044	0.599 ± 0.023	b	new
0631161222	01:26:24.73	−71:17:11.9	16.96	11435 ± 362	7.934 ± 0.059	0.569 ± 0.030	b	R22
0631344957	02:13:28.27	−64:37:08.9	16.98	11574 ± 311	7.995 ± 0.050	0.601 ± 0.026	b	R22
0640201450	03:21:09.03	+14:10:56.0	17.17	11979 ± 488	8.050 ± 0.070	0.632 ± 0.037	b	new
0661119673	04:42:58.31	+32:37:15.6	17.37	10668 ± 345	7.881 ± 0.082	0.540 ± 0.032	b	R22
0762000503	07:27:08.05	+14:52:16.2	17.22	11512 ± 339	8.015 ± 0.061	0.612 ± 0.032	b	new
0775564285	07:46:13.81	−30:25:50.9	16.03	10891 ± 211	7.938 ± 0.040	0.570 ± 0.020	b	new
0800126377	08:51:28.17	+06:05:51.1	16.82	11427 ± 37	8.128 ± 0.021	0.675 ± 0.012	i	new
...	...	...	...	11510 ± 227	7.957 ± 0.040	0.581 ± 0.020	b	...
0800420812	08:40:55.71	+13:03:29.4	17.19	11562 ± 225	7.981 ± 0.045	0.594 ± 0.023	b	new
0804835539	08:54:57.51	−76:46:21.9	16.91	15296 ± 476	8.078 ± 0.046	0.659 ± 0.051	b	R22
0842451090	10:21:32.75	+14:01:24.2	17.05	12191 ± 545	7.841 ± 0.067	0.525 ± 0.022	b	new
0900228144	11:01:21.93	+40:15:46.1	17.47	11410 ± 560	8.000 ± 0.110	0.604 ± 0.058	b	new
0900762564	11:37:38.38	+80:16:00.1	16.89	11939 ± 238	7.831 ± 0.035	0.524 ± 0.00	b	new
0902514572	11:43:19.10	-08:01:15.4	17.13	11449 ± 259	8.030 ± 0.050	0.620 ± 0.027	b	new
1102242692	15:28:09.27	+55:39:14.4	17.09	11180 ± 184	7.86 ± 0.07	0.531 ± 0.025	j	R22
1102346472	14:53:23.52	+59:50:56.2	17.16	12102 ± 345	8.067 ± 0.045	0.642 ± 0.024	b	R22
...	...	...	...	11217 ± 250	7.97 ± 0.038	0.589 ± 0.05	i	...
1860439362	19:21:54.59	+27:14:37.4	17.00	11809 ± 294	8.075 ± 0.044	0.646 ± 0.024	b	new
1944049427	20:38:04.29	+23:40:59.9	17.16	11338 ± 376	8.020 ± 0.065	0.614 ± 0.035	b	new
2045970633	23:45:07.33	+58:13:15.0	16.88	11570 ± 302	8.073 ± 0.049	0.644 ± 0.027	b	new

3. TESS DATA

We downloaded the 2-min and 20-s cadence light curves for all known white dwarfs and candidates for white dwarfs (Gentile Fusillo et al. 2019, 2021) brighter than G ≤ 17.5 mag from The Mikulski Archive for Space Telescopes, hosted by the Space Telescope Science Institute (STScI)[1] in FITS format. Data were processed on the basis of the Pre-Search data conditioning pipeline (Jenkins et al. 2016). The times and fluxes (PDCSAP FLUX) were extracted from the FITS files, with the times given in barycentric corrected dynamical Julian days (BJD – 2457000, corrected for leap seconds, see Eastman et al. 2010). The fluxes were converted to differential flux $\Delta I/I$, and then transformed to amplitudes in parts per thousand (ppt), which corresponds to the millimodulation amplitude unit (mma)[2]. Data were sigma-clipped at 5σ to remove outliers that depart from the median by 5σ.

We computed their Fourier transforms (FTs) looking for signatures of pulsations or binarity above the 1/1000 false-alarm probability (FAP). The FAP was calculated by reshuffling the data 1000 times, maintaining the same time base, and computing the Fourier transform, selecting the highest peak (see Kepler 1993, for details). Statistically, if a peak shows an amplitude above the FAP in the FT there is less than one chance in a 1000 that that given peak is due to

[1] http://archive.stsci.edu/

[2] 1 mma= 1/1.086 mmag= 0.1% = 1 ppt; see, e.g., Bognar & Sodor (2016).

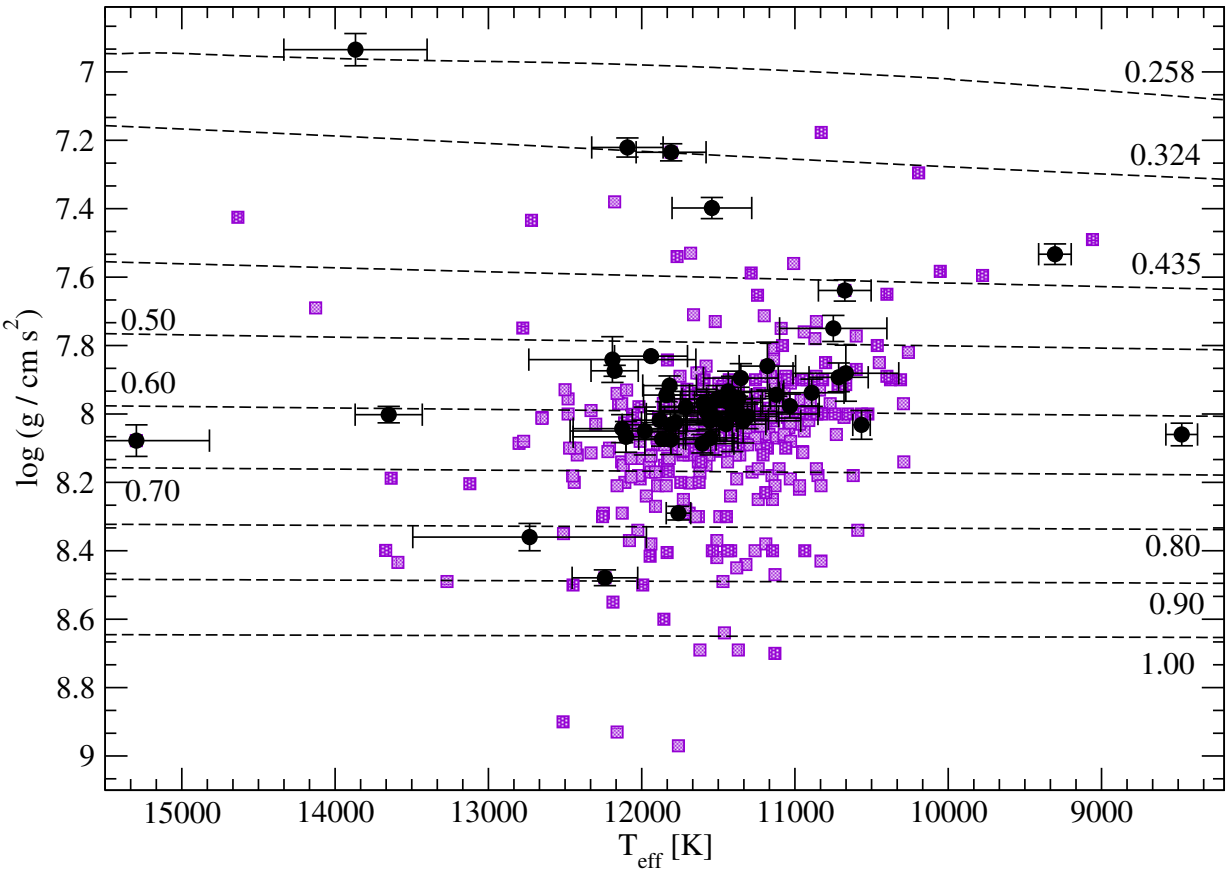

Figure 1. Distribution of ZZ Ceti stars on the $T_{\rm eff} - \log g$ plane. The purple squares correspond to the ZZ Ceti stars taken from Bognar & Sodor (2016); Hermes et al. (2017); Su et al. (2017); Romero et al. (2019b); Vincent et al. (2020) and Romero et al. (2022b). The objects of interest in this work are depicted with black circles. We include evolutionary tracks (dashed lines) with stellar masses between 0.435 $M_\odot$ and 0.9 $M_\odot$ from Romero et al. (2019a) and 0.258 and 0.324 $M_\odot$ from Istrate et al. (2014).

noise. For TESS data, the value of the FAP is of the order of $4\langle A\rangle$ for 120 s–cadence and $5\langle A\rangle$ for 20 s–cadence data (see Bischoff-Kim et al. 2014; Zong et al. 2016, for instance). For prewhitening, we used a nonlinear least squares (NLLS) method, by simultaneously fitting each pulsation frequency in a waveform $A_i \sin(\omega_1 t + \phi)$, with $\omega = 2\pi/P$ and P the period. This iterative process was performed starting with the highest amplitude peak until no peak appeared above the false alarm probability significance threshold of 0.1%. For objects showing only one variation period, we impose an amplitude at least 10 % above the FAP detection limit. We analyze the concatenated light curve from different sectors when observed, using the TESS-LS script.

The detection level of non–gaussian noise distribution is an active research area (see for example Kepler 1993; Sturrock & Scargle 2010; VanderPlas 2018; Vio et al. 2019). The most recommended determination for data with multiple periodicities and non-random noise, like that from the TESS satellite, is the randomization of the data, maintaining the timing sampling. The limit used is always a tradeoff between the detection of real periods and the exclusion of noise peaks. We analyzed the TESS data for over 9000 white dwarfs and over 400 known white dwarf pulsators. Our empirical best value is fap(1/1000). Considering any larger value excludes known pulsation periods, but lower values include noise peaks. Therefore, all the detections reported are for such a limit.

The flux corresponding to the white dwarf ranged from CROWDSAP = 0.021–0.985 due to the large pixel scale of the TESS plates, which means that the total flux from the white dwarf in the extracted aperture ranged from 2.1% to 98.5%. To confirm that the variations are from the white dwarf, we checked all stars around 120"x120" in Gaia EDR3 for other possible variables or parallax and proper motion companions. The values for the PDCSAP flux were corrected for crowding using the CROWDSAP value; thus, the reported amplitudes were corrected for flux dilution. For all objects in the sample, we run the TESS−localize software (Higgins & Bell 2023) to guarantee that the detected period arises from the white dwarf.

4. PERIODS AND DATA ANALYSIS

In this section, we present the results from the light curve analysis of all objects presented in Table 1, including 32

new bright ZZ Ceti stars. The period list for each object is presented in Tables 2 and 3 for the new ZZ Cetis, and the pulsating DA white dwarf stars reported by Romero et al. (2022b), respectively. We also include the sectors where each object was observed and the amplitude detection limit for the false alarm probability FAP=1/1000.

From the data obtained by TESS in Cycles 4 and 5, we found 20 new ZZ Ceti stars. As an example, we show the light curves and FT for TIC 0902514572 in Figure 2. The top panel shows the light curve for the data from Sector 46 with 120 s cadence, while the middle panel shows the data from Sector 63 with 20 s cadence. The bottom panel shows the FT for the concatenated data from both sectors, where there are three distinctive peaks above the detection limit of FAP (1/1000), indicated as a horizontal line at 16.60 ppt. The main peak is located at a frequency of $\sim 1200\,\mu$Hz, corresponding to a period ~ 830 s. Two objects were previously indicated as DAV stars. TIC 0014448610 was reported as a DAV pulsator by Vincent et al. (2020) with a detected period at 490 s. Using data from Sectors 44 to 46 we detected a total of 6 periods. Finally, Rowan et al. (2019) reported the detection of one period at ~ 490 s for TIC 0800420812, while we detect two periods at 507.76 and 333.75 s. The FT for the 32 new ZZ Ceti stars can be found in the Appendix 7.

For 12 objects, the data from the first three cycles, Sectors 1 to 39, lead to no pulsation-related variability detection, with peaks below the FAP(1/1000). However, new data from Cycles 4 and 5, particularly with 20 s cadence, led to the detection of pulsation variability in these objects.

From the sample of 74 new ZZ Cetis observed in the first three years of the TESS mission, analyzed by Romero et al. (2022b), there are 28 objects that were reobserved during the fourth and fifth cycles. Of these 28 targets, 21 of them showed a change in their period list, because of the reduction in noise. These 21 objects are listed in Table 3, where we also list the periods detected from the FT considering all observed sectors.

For most objects, the additional data lead to the detection of more periods, highlighted in italic in Table 3. For instance, for TIC 0317153172, three new low-amplitude periods were detected after data from Sectors 66 and 67 were included in the Fourier transform analysis. Figure 3 shows the FT for TIC 0317153172 from Sectors 27 and 39 on the top panel and for all sectors on the bottom panel. Note that three new peaks in the FT are above the FAP(1/1000) detection limit when data from the two sectors from Cycle 5 are included. In other cases, the additional periods correspond to components of rotational multiplets that were not resolved with the previous data. For instance, for TIC 1102242692, three components of a multiplet centered in 1009.03 s are above the detection limit, when 20-s-cadence data from Sectors 49 – 51 are considered.

For three objects, there is no observed variability above the FAP=1/1000 detection limit after further reobservation by TESS. TIC 0261400271 was reported to be variable by Romero et al. (2022b), showing two short periods of ~ 300s and ~ 380 s, with low amplitudes close to the detection limit. These periods are not present in the Fourier transform when 20-s data from Sectors 61, 62, and 64 are added to those from previous sectors; thus, we relabel this object as NOV in Table 3. Furthermore, Romero et al. (2022b) reported the detection of a peak from the FT of TIC 0804835539, and photometric variability was reported for TIC 0317620456 by Vincent et al. (2020) and Romero et al. (2022b). However, we found that the variability of these objects was probably coming from a nearby object in the large TESS pixels and not from the white dwarf; thus, they are also relabeled it NOV.

5. ASTEROSEISMOLOGICAL ANALYSIS

We analyzed the detected period list shown in Tables 2 and 3. Periods identified as components due to rotation, harmonics, and linear combinations are not taken into account in the asteroseismological fit, since we only consider $m = 0$ components in the computations of the theoretical periods. Rotational splitting is used to estimate rotation periods after a best-fit model is found.

For our seismological fit, we employ an updated version of the DA white dwarf model grid used in Romero et al. (2022b). DA white dwarf models were obtained from fully evolutionary computations using the stellar evolution code LPCODE (see Althaus et al. 2010; Renedo et al. 2010; Romero et al. 2015, for details). The computations start in the zero-age main sequence, going through the central hydrogen and helium burning stages and the giant phases, where the mass loss episodes occur. In particular, we compute the Thermally Pulsing AGB phase, where most of the mass is lost to the interstellar medium. Finally, after the evolution during the post-AGB phase, where the effective temperature increases rapidly at almost constant luminosity, the computations arrive at the white dwarf cooling sequence. We computed the evolution through the cooling curve, including the DA instability strip between $\sim 12\,500$ and $\sim 10\,000$ K. The computations start at the main sequence with $Z = 0.01$ and stellar masses from 0.8 $M_\odot$ to 6.7 $M_\odot$, leading to white dwarf masses between 0.493 $M_\odot$ to 1.05 $M_\odot$. The stellar mass values of our complete model grid are listed in Column 1 of Table 4, along with the hydrogen (Column 2) and helium (Column 3) content as predicted by standard stellar evolution, and the central oxygen abundance by mass (X_O) in Column 4. Note that the parameters for each white dwarf mass listed in table 4 are not free parameters but determined by detailed evolutionary computations from the zero-age main sequence to the white dwarf cooling curve. For instance, the amount of carbon and oxygen in the core is fixed by the helium nuclear burning in

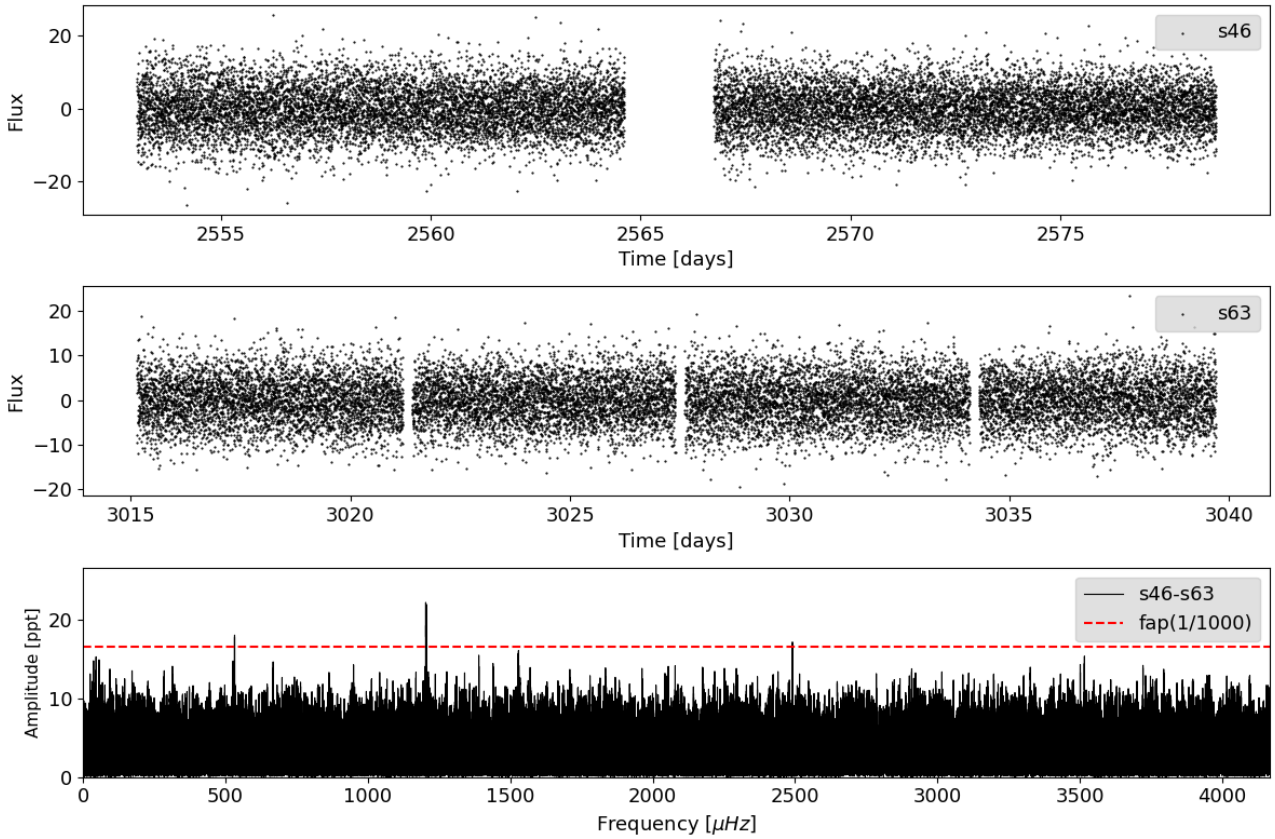

Figure 2. Light curves from sectors 46 (120s–cadence) and 63 (20s–cadence) for TIC 0902514572, shown in the top and middle panel, respectively. The bottom panel presents the Fourier transform of the concatenated data. The horizontal red line corresponds to the false-alarm probability FAP=1/1000 detection limit.

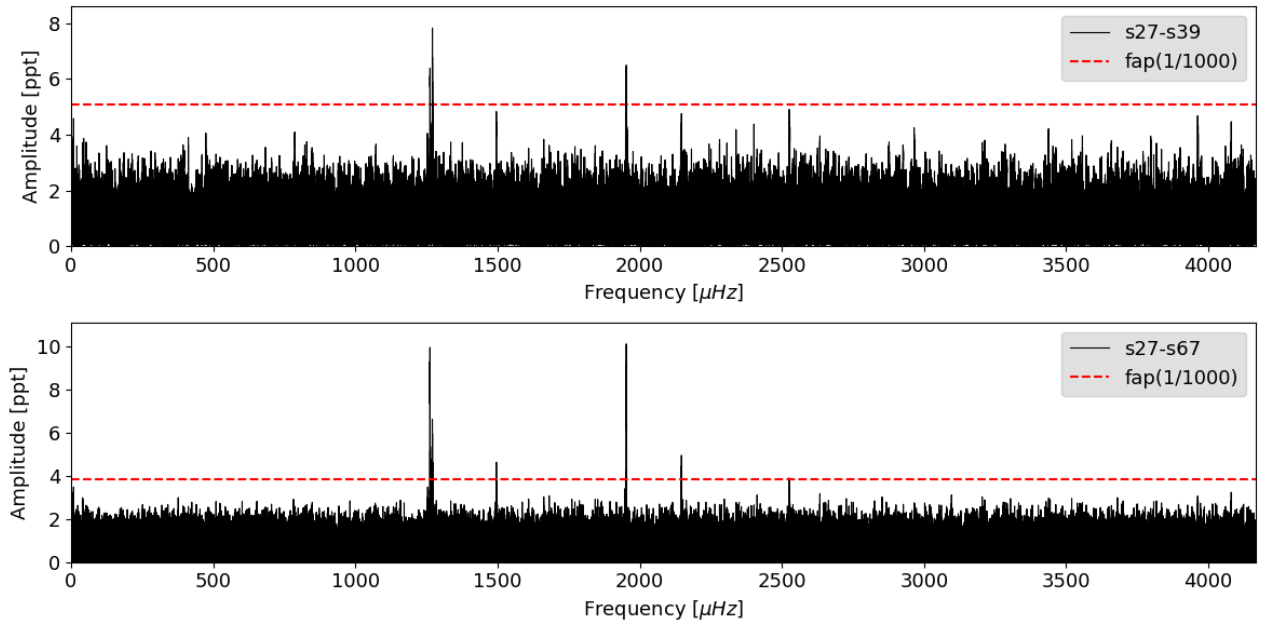

Figure 3. Fourier transform for the data for TIC 0317153172 data for sectors 27 to 39 (top panel), and for sectors 27 to 67 (bottom panel). The horizontal red line corresponds to the false-alarm probability FAP=1/1000 detection limit.

Table 2. Detected periods for the 32 new ZZ Cetis from TESS. For each object, we list the sectors where the target was observed by TESS, indicating the 20 s cadence runs with "f" (Column 2), the value of the amplitude detection limit for false-alarm probability FAP(1/1000) (Column 3), the CROWDSAP value (Column 4) and the list of periods compatible with stellar pulsations in white dwarfs (Column 5). We truncate all periods to two decimal places only because the uncertainties in the theoretical models are of the order of 1 s.

TIC	Sector(s)	FAP(1/1000) [ppt]	CROWDSAP	Π (Amp) [s] ([ppt])
0001116746	f48	7.24	0.803	303.0079 (8.61)
0014448610	f44-46	2.84	0.048	472.1259 (5.42), 496.9143 (4.89), 634.3407 (4.70),
...	...	...	...	679.2715 (3.47), 527.9240 (3.08), 373.5692 (3.04)
0030545382	11,f37,f64	3.59	0.113	1160.5361(9.82), 781.5003 (8.89), 718.1825 (5.15),
...	...	...	...	1141.2900 (4.90)
0072517198	f50	8.73	0.386	848.9142 (14.28)
0081848974	f36-f37,f63-f64	7.01	0.038	874.5769 (9.52)
0088046487	f45	5.62	0.886	632.1540 (11.28), 885.7615 (8.64), 829.8511 (6.20)
0094748632	f44-f46	3.86	0.590	306.9730 (6.28), 257.6284 (5.69)
0103700861	f40-f41,f47	4.50	0.329	536.9214 (5.54), 715.8960 (4.59)
0114058447	f42-f44	2.73	0.104	1402.6479 (6.70), 1400.9989 (3.28), 319.9132 (2.92)
0141179495	22,f49	3.87	0.930	253.8587 (4.46)
0159973152	31	5.444	0.306	977.5500 (7.27), 922.3300 (6.43), 1023.4800 (6.07)
0192937035	20,47,f60	4.55	0.070	298.2742 (5.25)
0201860926	29-30,69	4.40	0.518	893.7354 (6.82), 880.7364 (7.31), 525.0553 (5.89),
...	...	...	...	522.7729 (4.89), 520.4211 (7.53), 486.0465 (4.49)
0264172524	14-16,18-26,f40-f41,f47-f51,f53-f60	2.45	0.278	463.07855 (5.69), 336.2565 (2.78), 847.8119 (2.62)
0375199799	f55	9.17	0.102	328.1167 (9.56),305.5302 (12.98)
0409732714	34,f61	1.34	0.721	448.2355 (1.51), 940.4772 (1.26)
0423658036	10,f37,f64	3.637	0.753	372.3161 (4.344)
0453210132	34,f44-f46	5.85	0.362	200.3091 (6.93)
0461203226	f37,f64	3.73	0.048	297.7803 (4.39), 259.9130 (10.29)
0600589802	f57	8.14	0.102	959.0156 (25.88), 966.9947 (8.87), 868.6355 (17.20),
...	...	...		530.1465 (12.13), 479.6121 (8.37)
0640201450	42-44	11.03	0.630	254.8758 (13.59)
0762000503	44-46	10.04	0.096	453.6563 (15.26), 299.2025 (13.70), 1427.6855 (10.18)
0775564285	f61	8.25	0.064	852.9632 (12.34), 895.8052 (9.04), 627.8357 (10.19)
0800126377	f44-f45,61	8.14	0.061	325.0489 (10.18), 326.3151 (9.26)
0800420812	44-46	10.87	0.423	507.7647 (23.31), 333.7467 (10.84)
0842451090	45-46	7.42	0.871	311.8042 (10.51)
0900228144	48	15.99	0.326	578.1738 (29.82), 826.5413 (28.02), 542.7727 (18.81)
0900762564	f40-41,47,f53,f60	4.32	0.116	268.3894 (5.12), 260.78 00(4.61), 885.5552 (4.33)
0902514572	46,f63	16.60	0.421	831.1278 (22.21), 829.5588 (21.94), 1879.2114 (18.11),
...	...	...	...	401.5154 (17.24)
1860439362	41,54	43.86	0.039	575.2658 (88.17), 461.7913 (67.71)
1944049427	41,55	43.83	0.090	606.2664 (85.79)
2045970633	17,24,f57-f58	26.43	0.063	883.6108 (28.82), 930.0163 (27.01), 726.4908 (26.10)

Table 3. List of stars identified as ZZ Cetis by Romero et al. (2022b) using data from Sector 1 to Sector 39, showing a change in the period list when data from Sectors 40 to 69 are added to the analysis. We list TIC (column 1), all sectors where they were observed (column 2), the detection limit FAP(1/1000) (column 3), the CROWDSAP value (Column 4) and all detected periods (column 5). The periods detected after the new data were added to the FT are in italics. We truncate all periods to two decimals places only because the uncertainties in the theoretical models are of the order of 1 s.

TIC	Sector(s)	FAP(1/1000) [ppt]	CROWDSAP	Π (Amp) [s] ([ppt])
0007675859	25,26,f40,f52-f54	4.09	0.184	798.6466 (4.72), 743.4557 (4.30), *575.4137 (5.87)*,
...	...	...		356.0961 (5.26), 353.2529 (10.5), *254.4896 (4.14)*
0021187072	25,26,f40-f41,f52-f54	3.13	0.394	1076.9291 (4.13), *887.4689 (3.32)*, *823.6757 (3.25)*,
...	...	...	...	*794.2685 (3.13)*, *776.7064 (3.56)*
0033717565	27-29,32,35-36,39,f61-f63,f65-f68	1.71	0.712	364.9195 (9.30), 526.9731 (6.08), *243.0180 (2.04)*,
...	...	...	...	*703.7792 (1.74)*, *615.1347 (1.74)*, *484.1677 (1.76)*,
...	...	...	...	*460.5366 (1.77)*
0055650407	11-13,f27-f39,f61-f64	0.36	0.965	320.7647 (1.59), *318.0155 (0.59)*, 262.4567 (7.19),
...	...	...	...	*261.6101 (0.47)*, *206.7012 (0.39)*, *200.6561 (0.88)*,
...	...	...	...	200.0848 (4.42), *199.5171 (0.59*, *153.2654 (0.41)*,
...	...	...	...	*127.0289 (0.48)*, 126.8410 (1.80)
0063281499	01,f28,f68	2.071	0.707	383.7004 (2.73), 320.5148 (7.40), *269.1340 (2.31)*
0079353860	01, 27, 67	2.13	0.466	*982.0192 (2.34)*, 945.15 27(2.63), 525.5468 (2.37)
0149863849	f39,f66	1.49	0.146	*835.8379 (2.08)*, *810.9993 (1.58)*, *804.0059 (1.51)*,
...	...	...	...	*800.0012 (3.14)*, *796.0475 (1.53)*, *789.2699 (3.27)*,
...	...	...	...	*769.6706 (1.99)*, *763.4047 (3.48)*, *759.7776 (9.91)*,
...	...	...	...	*756.1906 (2.80)*, *750.0885 (4.59)*, *660.6219 (2.43)* ,
...	...	...	...	568.0883 (1.96), 491.2130 (4.09), 487.3459 (1.94),
...	...	...	...	398.9574 (10.3) *389.6772 (2.39)*, *379.8913 (3.30)*,
...	...	...	...	*261.1825 (1.69)*
0230384389	14-26,f40-f41,f47-f54,f56-f60	0.47	0.668	*756.8263 (0.71)* , *753.0697 (0.85)*, 749.6259 (0.74),
...	...	...	...	707.9282 (1.41), 707.9282 (1.41), *494.7838 (0.90)*,
...	...	...	...	493.86 (0.85), 457.1689 (1.32), 1633.5816 (0.59)
0261400271	1,4,7,8,11-13,f27-f28,f31,f34,	0.49	0.632	NOV
...	f38-f39,f61-f62,f64	...	...	...
0273206673	19,f59	8.02	0.178	*941.8324 (8.20)*, *914.8126 (12.60)*, 892.9687 (10.01),
...	...	...	...	874.5539 (7.44), 844.0813 (9.07), 827.1640 (16.81),
...	...	...	...	*826.4667 (14.44)*, *825.3140 (9.96)*, 746.6810 (10.26),
...	...	...	...	698.8889 (10.46), 688.9567 (8.06), 663.2466 (8.41),
...	...	...	...	698.8889 (10.46), 688.9567 (8.06), 663.2466 (8.41),
...	...	...	...	583.4373 (17.43), 511.4147 (10.91), 464.4207 (9.59)
0304024058	10-11,f36-f38,f63-f64	3.54	0.375	*740.9767 (3.73)*, 623.2835 (5.49), 579.4716 (13.05),
...	...	...	...	506.1983 (11.54), 400.2769 (12.32)
0317153172	27,f39,f66-67	3.81	0.526	792.0666 (9.94), 786.8873 (6.59), *668.3902 (4.63)*,
...	...	...	...	512.0485 (10.01), *465.7770 (4.98)*, *395.9408 (3.89)*
0317620456	26,f40,f53-f54	4.16	0.126	NOV
0343296348	12-13,f39,f66	4.41	0.358	288.2725 (10.81), *287.2597 (7.11)*
0353727306	18-19,25,f52,f58-f59	5.00	0.386	*876.0786 (8.10)*, *873.8737 (8.94)*, *771.3014 (5.22)*,
...	...	...	...	*750.8409 (5.49)*, *729.8417 (5.48)*, 545.8157 (22.0),
...	...	...	...	470.2363 (9.35), 463.5429 (5.70), 404.8402 (8.54),
...	...	...	...	*399.5620 (5.07)*
0631161222	27,29,f68	5.59	0.336	707.9696 (15.80), 679.8159 (26.27), 466.6203 (10.29),
...	...	...	...	403.6266 (12.45), 367.4430 (8.35), *346.7911 (6.16)*
0631344957	28-29,f68	6.23	0.840	363.1425 (7.94), *313.4443 (6.44)*
0661119673	19,43-44,f59	18.34	0.163	626.3703 (46.78), $2f_1$ =*313.1050 (19.11)*
0804835539	37-39,f64-f66	6.04	0.114	NOV
1102242692	16,22,24,f49-f51	4.89	0.900	*1015.0376 (5.73)*, 1009.0271 (8.37), *1003.0941 (4.94)*
1102346472	15-16,22-23,48-50	6.93	0.329	458.1267 (23.45), *1489.6526 (7.27)*

the horizontal branch, the value for the helium layer is determined by residual H and He shell-burning stages and the number of thermal pulses during the TP-AGB stage. The value of the hydrogen mass listed in table 4, corresponds to the maximum amount of hydrogen that can be left on top of a white dwarf, indicated as canonical from now on, and is determined mainly by the residual burning during the post-AGB stage (see Romero et al. 2019a, for details).

The third free parameter in our white dwarf model grid corresponds to the hydrogen mass at the white dwarf stage. Evidence of the existence of white dwarf stars with thin hydrogen envelopes (thinner than the canonical value) have been presented in the literature. For instance, Althaus et al. (2005) have found that the amount of hydrogen left in a DA white dwarf can be significantly reduced if the progenitor star experiences a late thermal pulse. In fact the value of M_H was estimated for 40 Eridani B, using independent determinations for its radius and mass, being below $\sim 10^{-8} M_*$ (Bond et al. 2017; Romero et al. 2019a). White dwarf cooling sequences with lower values of M_H were computed from the canonical models by replacing H by He at the base of the hydrogen envelope. This is done at high effective temperatures ($> 70\,000$ K), so that any transitory effects associated with this procedure end long before the models reach the stage of pulsating DA white dwarfs.

The first version of the model grid was presented in Romero et al. (2012), consisting of C/O-core white dwarf models with 11 different stellar masses between 0.525 $M_\odot$ and 0.878 $M_\odot$, and 6 to 8 different values of the hydrogen envelope mass, depending on the stellar mass. The grid was extended to higher masses, up to 1.05 $M_\odot$ by Romero et al. (2013), who added 6 additional sequences. In further work, the grid was extended by adding models with different stellar masses and hydrogen envelopes (Romero et al. 2017, 2019b). The current model grid is composed of 30 stellar mass values between 0.493 $M_\odot$ to 1.05 $M_\odot$, with a hydrogen envelope mass in the range of $\sim 3.5 \times 10^{-4}$ to $\sim 10^{-10}$ M_*, adding to a total of 611 cooling sequences.

For hydrogen envelopes thinner than $M_H/M_* = 10^{-10}$ it is expected that the outer convective zone will mix hydrogen into the more massive helium layer before reaching the ZZ Ceti instability strip, turning the star into a DB white dwarf (Ourique et al. 2020; Cunningham et al. 2020).

Nonradial adiabatic g-mode pulsations were computed for models with effective temperatures from 13 500 K to 9 500 K, using the adiabatic version of the LP-PUL pulsation code (see Córsico & Althaus 2006, for details). We consider dipolar ($\ell = 1$) and quadrupolar ($\ell = 2$) modes with periods up to 2000 s.

For each object, we searched for an asteroseismologically representative model that best matches the observed periods.

Table 4. Main Characteristics of DA WD Models Set. We list the stellar mass at the white dwarf cooling curve (Column 1), the canonical mass of hydrogen (Column 2) and helium (Column 3), i.e. those resulting from stellar evolution calculations, and the amount of oxygen at the core (Column 4)

$M_*/M_\odot$	$-\log(M_H/M_*)$	$-\log(M_{He}/M_*)$	X_O
0.493	3.50	1.08	0.720
0.510	3.53	1.19	0.703
0.525	3.62	1.31	0.709
0.534	3.65	1.38	0.677
0.542	3.68	1.35	0.685
0.548	3.74	1.38	0.697
0.550	3.65	1.39	0.698
0.560	3.70	1.42	0.691
0.570	3.82	1.46	0.696
0.580	3.86	1.57	0.698
0.593	3.93	1.62	0.704
0.609	4.02	1.61	0.723
0.621	4.04	1.68	0.732
0.632	4.25	1.76	0.755
0.646	4.12	1.83	0.742
0.660	4.26	1.92	0.730
0.674	4.35	1.97	0.707
0.686	4.35	2.03	0.711
0.690	4.46	2.04	0.684
0.705	4.45	2.12	0.661
0.721	4.50	2.14	0.659
0.745	4.62	2.18	0.657
0.771	4.70	2.23	0.655
0.800	4.84	2.33	0.648
0.820	4.93	2.41	0.639
0.837	5.00	2.50	0.640
0.860	5.08	2.55	0.624
0.878	5.07	2.59	0.611
0.900	5.28	2.72	0.609
0.917	5.41	2.88	0.609
0.949	5.51	2.92	0.614
0.976	5.68	2.96	0.613
0.998	5.70	3.11	0.629
1.024	5.74	3.25	0.631
1.050	5.84	2.96	0.613

To this end, we seek for the theoretical model that minimizes the quality function,

$$\chi^2(M_*, M_{\rm H}, T_{\rm eff}) = \frac{1}{N-1} \sqrt{\sum_{i=1}^{N} \min \left[\Pi_i^{\rm th} - \Pi_i^{\rm obs}\right]^2}, \quad (1)$$

where N is the number of observed periods, $\Pi_i^{\rm th}$ is the theoretical period that best fits the observed period $\Pi_i^{\rm obs}$ in the

model. When the star only shows one period, we set the factor $1/(N-1)$ to one. For the period fit, we consider only periods identified as $m = 0$ modes. Thus, we do not consider periods corresponding to harmonics or linear combinations, or other components from rotational multiplets. For stars with a spectroscopic or photometric mass below the minimum value of our C/O-core grid (0.493 $M_\odot$) we also perform a preliminary asteroseismological fit with He–core white dwarf models with stellar masses from 0.17 to 0.45 $M_\odot$ (Córsico et al. 2012), considering only thick hydrogen envelopes, as predicted by the previous evolution, and $\ell = 1$ modes. External constraints are considered in the fitting procedure especially for objects that show only one or two periods. For example, the values of the effective temperature and stellar mass determinations in Table 1 are taken into account as additional restrictions. Also, the presence of multiplets gives additional information on the harmonic degree of a given period, which is also considered in the fitting process. 25However, note that some particular short periods ($\lesssim 200$ s) can be strong constraints on their own, since they propagate in the inner parts of the star and are particularly sensitive to the inner structure.

The results of our asteroseismological fits are presented in Table 5 for all objects analyzed in this work. The values for the stellar mass, the thickness of the hydrogen envelope, and the effective temperature for the seismological model are listed in columns 2, 3, and 4, respectively. In column 5 we list the values for the theoretical periods that better fit the observed periods, along with the corresponding harmonic degree ℓ and the radial order k. The value of the quality function χ^2 is shown in column 9 for objects showing more than one period. The first model listed is the one we choose to be the best-fitting model for that particular object.

Table 5. Best fit model for the 50 ZZ Cetis analyzed in this work using the list of observed modes. The stellar mass, hydrogen envelope, and effective temperature are listed in columns 2, 3, and 4, respectively. We list the theoretical periods in Column 5, along with the harmonic degree and the radial order. The value of the quality function χ^2 in seconds is listed in Column 6, for objects with more than one period.

TIC	$M/M_\odot$	$-\log(M_H/M_*)$	$T_{\rm eff}$ [K]	Π[s] (ℓ, k)	χ^2 [s]
0001116746	0.609	4.02	12080	303.02 (1,5)	···
0007675859	0.900	8.37	12180	355.26 (1,6), 575.22 (1,12), 799.07 (1,18), 743.19 (2,30), 253.69 (1,45)	0.58
0014448610	0.609	4.97	11510	428.67 (1,7), 492.59 (1,9), 634.65 (2,23)	0.96
···	···	···	···	676.63 (2,25), 531.04 (2,19), 371.74 (2,12)	···
0021187072	0.542	5.43	11740	1077.96 (1,19), 884.93 (2,27), 824.14 (2,24), 776.69 (1,13)	0.73
0030545382	0.534	6.83	11800	1161.46 (1,19), 780.01 (1,12), 718.35 (1,11), 1137.87 (2,33)	1.25
0033717565	0.570	8.31	11600	366.26 (1,4), 524.82 (1,7), 241.38 (2,5), 458.28 (2,12)	0.75
···	···	···	···	482.95 (2,13), 616.99 (2,17), 704.82 (2,20)	
0055650407	0.570	3.92	12380	263.94 (1,3), 204.97 (2,5), 125.53 (1,1), 319.56 (1,5), 153.35 (2,3)	1.35
···	0.593	3.93	11630	262.18 (1,3), 193.95 (1,2), 121.80 (1,1), 314.04 (1,5),152.15 (2,3)	2.62
0063281499	0.570	7.83	12000	319.05 (1,3), 384.69 (1,50, 269.22 91,2)	0.60
0072517198	0.510	6.33	11000	848.92 (1,3)	···
0079353860	0.690	8.38	11370	981.62 (1,18), 945.68 (1,17), 526.50 (1.8)	0.56
0081848974	0.570	5.47	11120	874.56 (1,15)	···
0088046487	0.660	4.25	11370	632.33 (1,13), 885.36 (1,19), 830.12 (2.32)	0.25
0094748632	0.593	3.93	12350	306.99 (1,5), 257.68 (1,3)	0.01
0103700861	0.705	7.35	10190	537.03 (1,8), 715.98 (1,12)	0.11
0114058447	0.593	7.34	11520	1400.80 (1,25), 320.31 (1,4)	0.45
···	0.358	3.18	9470	1400.03 (1,21), 335.90 (1,3)	16.02
0141179495	0.632	6.34	11690	253.86 (1,3)	···
0149863849	0.660	4.24	11590	839.63 (1,18), 798.34 (1,17), 760.54 (1,16), 658.46(2,25),	1.06
···	···	···	···	568.16 (1,11), 492.30 (2,18), 486.85 (1,10), 402.11 (1,7), 383.53 (2,13)	···
0159973152	0.542	6.83	10450	977.63 (1,15), 922.01 (2,25), 1023.50 (2,28), 0.17	

Table 5 *continued*

Table 5 *(continued)*

TIC	$M/M_\odot$	$-\log(M_H/M_*)$	T_{eff} [K]	Π[s] (ℓ, k)	χ^2 [s]
···	0.570	9.33	11210	976.71 (1,15), 921.76 (1,14), 1024.25 (1,16)	0.64
0192937035	0.550	3.65	11830	298.22 (1,4)	···
···	0.450	3.43	11640	298.18 (1,3)	···
0201860926	0.534	6.13	11280	879.13 (1,14), 522.82 (1,7), 486.32 (2,13)	0.81
0230384389	0.660	5.85	11660	707.50 (1,13), 456.69 (1,7), 493.99 (1,8), 753.78 (1,14), 1635.17 (2,56)	0.51
0264172524	0.686	5.55	12300	462.85 (1,8), 337.44 (1,5), 848.23 (1,17)	0.64
0273206673	0.705	5.26	11280	584.85 (1,11), 699.51 (1,14), 746.95 (1,15), 829.54 (1,17),	0.75
···	···	···	···	463.45 (2,16), 509.82 (2,18), 664.26 (2,24), 683.93 (2,25),	···
···	···	···	···	845.79 (2,31), 888.78 (2,33), 916.13 (2,34), 944,73 (2,35)	···
···	0.675	4.87	11310	587.57 (1,11), 698.45 (1,14), 748.89 (1,15), 831.58 (1,17),	0.86
···	···	···	···	464.03 (2,16), 510.09 (2,18), 664.03 (2,24), 690.29 (2,25),	···
···	···	···	···	837.84 (2,31), 891.14 (2,33), 916.11 (2,34), 941.67 (2,35)	···
0304024058	0.609	4.95	11210	581.61 (1,10), 396.42 (1,6), 505.12 (1,8), 624.53 (1,11), 738.84 (2,25	1.29
···	0.593	6.33	11360	579.01 (1,9), 401.61 (2,11), 507.23 (2,15), 624.14 (2,19), 739.53 (2,23)	0.61
0317153172	0.686	4.43	11920	794.04 (1,17), 787.36 (2,30), 668.27 (1,14), 511.24 (1,10),	0.44
···	···	···	···	464.86 (1,14), 395.88 (1,7)	···
0343296348	0.548	4.27	11310	287.77 (1,3)	···
0353727306	0.621	4.04	11470	872.48 (1,18), 775.95 (2,29), 752.41 (2,28), 729.70 (1,15)	1.71
···	···	···	···	538.20 (1,10), 467.11 (1,8), 408.31 (1,7)	···
···	0.690	6.25	11310	874.43 92,30), 765.15 (2,26), 751.76 (1,14), 733.20 (2,25),	1.24
···	···	···	···	543.99 (1,9), 468.88 (2,15), 404,66 (2,15)	···
0375199799	0.570	4.08	11810	305.21 (1,4), 328.12 (1,5)	0.34
0409732714	0.542	6.23	12200	448.23 (1,6)	···
0423658036	0.623	8.33	13700	372.31 (1,5)	···
···	···	···	···	568.16 (1,11), 486.85 (1,10), 492.30 (2,18), 402.12 (1,7), 383.53 (2,13)	
0453210132	0.593	5.64	12100	200.34 (1,2)	···
0461203226	0.560	3.70	11990	256.79 (1,3), 298.06 (1,4)	0.30
0600589802	0.609	4.56	11560	952.54 (1,19), 866.63 (1,17), 560.32 (2,18), 969.17 (2,35), 479.04 (2,16)	0.76
0631161222	0.609	5.44	11430	707.54 (1,13), 678.27 (1,12), 466.56 91,7), 402.97 (1,6),	0.60
				368.25 91,5), 349.06 (2,10)	···
0631344957	0.593	5.14	11230	362.62 (1,5), 313.35 (1,4)	0.53
0640201450	0.686	4.43	12280	254.88 (1,4)	···
0661119673	0.570	4.55	11600	626.42	···
0762000503	0.646	4.12	11830	453.37 (1,8), 299.40 (1,5), 1429.62 (2,57)	0.98
0775564285	0.525	3.62	11600	852.63 (1,16), 628.41 (1,11) 895.85 (1,17)	0.33
0800126377	0.570	4.84	11550	325.04 (1,4)	···
0800420812	0.593	4.84	11470	507.74 (1,8)	···
0842451090	0.534	3.97	12000	311.72 (1,4)	···
0900228144	0.686	4.87	11660	579.33 (1,11), 826.69 (1,17), 542.95 (2,19)	0.59
0900762564	0.525	3.62	11930	268.28 (1,2), 885.66 (1,17)	0.16
0902514572	0.548	3.68	11370	830.59 (1,16), 653.86 (1,12), 486.96 (1,8)	0.41

Table 5 *continued*

Table 5 *(continued)*

TIC	$M/M_\odot$	$-\log(M_H/M_*)$	T_{eff} [K]	Π[s] (ℓ, k)	χ^2 [s]
1102242692	0.609	5.44	11200	1009.13 (1,19)	···
1102346472	0.548	7.33	11470	458.04 (1,6), 1489.63 (2,45)	0.01
1860439362	0.621	4.04	11760	574.97 (1,11), 462.26 (1,8)	0.55
1944049427	0.593	7.34	11370	606.26 (1,9)	···
2045970633	0.690	5.23	11560	883.35 (1,18), 930.00 (1,19)	0.26

5.1. *Rotation*

White dwarf stars are generally considered slow rotators, with rotation periods between a few hours and several days (see for instance Kepler & Romero 2017). From a sample of 116 white dwarfs, Da Rosa et al. (2024) found that the most probable rotation period is 3.9 h. By considering the frequency splitting, we can estimate the rotation period of the white dwarf star, following equation (Cowling & Newing 1949; Ledoux 1951):

$$\frac{1}{P_{\rm rot}} = \frac{\Delta\nu_{k,\ell,m}}{m(1 - C_{k\ell})}, \tag{2}$$

where m is the azimuthal number, $\Delta\nu_{k,\ell,m}$ is the frequency separation and $C_{k\ell}$ is the rotational splitting coefficient given by:

$$C_{k,\ell} = \frac{\int_0^{R_*} \rho r^2 [2\xi_r\xi_t + \xi_t^2] dr}{\int_0^{R_*} \rho r^2 [\xi_r^2 + \ell(\ell+1)\xi_t^2] dr}, \tag{3}$$

where ρ is the density, r is the radius, and ξ_r and ξ_t are the radial and horizontal displacement of the material.

Considering that all our datasets have very high duty cycles, the TESS data are generally free of aliasing, and patterns of even frequency spacing in the Fourier transform can appear, which opens the opportunity to estimate the stellar rotation rate (e.g., Kawaler 2004). Identifying rotationally split multiplets can also lead to the identification of the spherical degree ℓ and azimuthal order m of the modes present in the period spectrum (e.g., Winget et al. 1991, 1994).

Using the combined data from the first five years of TESS, we identified multiplets, both triplets and doublets, in the period spectrum of 9 objects studied in this work. For four objects, we detected more than one multiplet. When doublets appear, we consider that the component with the largest amplitude corresponds to the $m = 0$ component of the multiplet, while the second component corresponds to a $m = \pm 1$ component, unless otherwise stated (Brassard et al. 1995). A list of the 9 objects and all detected multiplets is presented in Table 6, together with the frequency separation, the frequency of the central component $m = 0$, the value of the rotational splitting coefficient $C_{k\ell}$ obtained from the representative asteroseismological model listed in Table 5, the corresponding rotation period in hours, calculated from Equation 2, and a label indicating whether the multiplet is a doublet (D) or a triplet (T). All $m = 0$ modes are fitted with a theoretical $\ell = 1$ mode, except the mode with a frequency of 4998.00 μHz corresponding to TIC 0055650407, and the mode with frequency 2035.58 μHz corresponding to TIC 0149863849, that are better fitted by a $\ell = 2$ mode.

Table 6. List of objects with detected rotational splitting. For each object, we list the TIC number (Column 1) the frequency separation $\Delta\nu$ (Column 2), the frequency of the $m = 0$ central component (Column 3), the value of the $C_{k\ell}$ obtained from the asteroseismological representative model (Column 4), and the mean rotation period (Column 5). The last column indicates if the observed multiplet is a doublet (D) or a triplet (T).

TIC	$\Delta\nu$ [μHz]	$\nu_{m=0}$ [μHz]	$C_{k\ell}$	$\bar{P}_{\rm rot}$ [h]	
0007675859	22.66	2830.83	0.4172	7.15	D
0055650407	11.79	7883.95	0.4853	12.12	D
···	14.24	4998.00	0.1012	17.54	T
···	12.38	3810.10	0.4717	11.85	D
···	13.48	3131.08	0.3817	12.74	D
0079353860	8.51	1902.77	0.4775	17.06	D
0149863849	16.15	2035.58	0.1574	14.49	D
···	6.25	1316.17	0.4907	22.64	T
···	6.22	1250.00	0.4910	22.73	T
0201860926	16.51	1135.41	0.4865	8.64	D
···	8.48	1912.56	0.4938	16.58	T
0343296348	12.20	3468.97	0.4576	12.35	T
0353727306	32.64	2470.11	0.4871	4.65	D
···	30.74	2126.57	0.4853	4.37	D
0800126377	11.94	3076.46	0.3512	15.10	D
1102242692	5.78	991.05	0.4900	24.14	T

Figure 4 shows the FT for the four multiplets detected for TIC 0055650407. For this object, we consider the components of the doublet at ~ 262 s to correspond to the components of $m = \pm 1$, and thus the multiplet would be centered at a frequency of 3131.08 μHz. The period with ~200 s (4998.00 μHz) is identified as a $\ell = 2$ mode in the representative asteroseismological model, giving a rotation period of

17.54 h. If we consider an alternative identification, as an ℓ=1, k=2 mode, with a $C_{k\ell}$ = 0.3719, the resulting rotation period would be 12.25 h, closer to the values obtained for the other three multiplets observed for this object.

TIC 0149863849 (fig. 5) has a complex structure of multiplets centered at 759.78 s and 800.00 s. In addition, there are two doublets, the more prominent being the one corresponding to the largest amplitude peak at 398.96 s.

TIC 0201860926 (fig. 11) shows a doublet and a triplet that lead to rotation periods of 8.64 and 16.58 h. Note that if we identify the two components of the doublet as $m = \pm 1$ both multiplets would indicate a similar rotation period.

A second possible solution is listed for TIC 0353727306 (fig. 7) in Table 5 where the periods identified as multiplets are represented by theoretical modes with $\ell = 2$. If we consider this solution, the mean rotation period for this object is 7.45 h (14.90 h), when the components are considered to be $m = 1$ ($m = 2$).

For TIC 0202860926 we detect two multiplets, one triplet and one doublet. Note that the rotation period computed from the doublet, considering the components to be $m = 0$ and $m = \pm 1$ is 8.64 h, near half the value obtained from the triplet. This could be indicating that the detected peaks are in fact $m = \pm 1$ components, if we consider a small rotation gradient.

Finally, TIC 0007675859 (Fig. 9), TIC 0079353860 (Fig. 10), TIC 0343296348 (Fig. 11), TIC 0800126377 (Fig. 12) and TIC 1102242692 (Fig. 13) show only one detected multiplet, leading to rotation periods from 7.15 h to 24.14 h.

Figure 14 shows the rotation period distribution obtained from asteroseismology as a function of stellar mass for the sample of 41 DA white dwarf stars. The purple dots correspond to data from the literature (see Da Rosa et al. 2024, for details), while the black squares correspond to the values listed in Table 6. For objects with more than one multiplet, we plot all values. Note that the values for the rotation periods agree well with those in the literature in the mass–period diagram. The mean value for the rotation period for the nine objects from Table 6 is 13.6 h. This value is significantly lower than the mean rotation period of 36.1 h obtained for the sample of 41 DA white dwarfs presented in Da Rosa et al. (2024). Thus, the mean rotation period for DA white dwarfs obtained from asteroseismology is reduced when the data from TESS is included.

6. ANALYSIS OF THE SAMPLE

In this section, we analyze the results from the periods and structure parameter for the 105 pulsating DA white dwarf stars that have been identified from the TESS data in the first five years.

6.1. *Stellar mass and effective temperature*

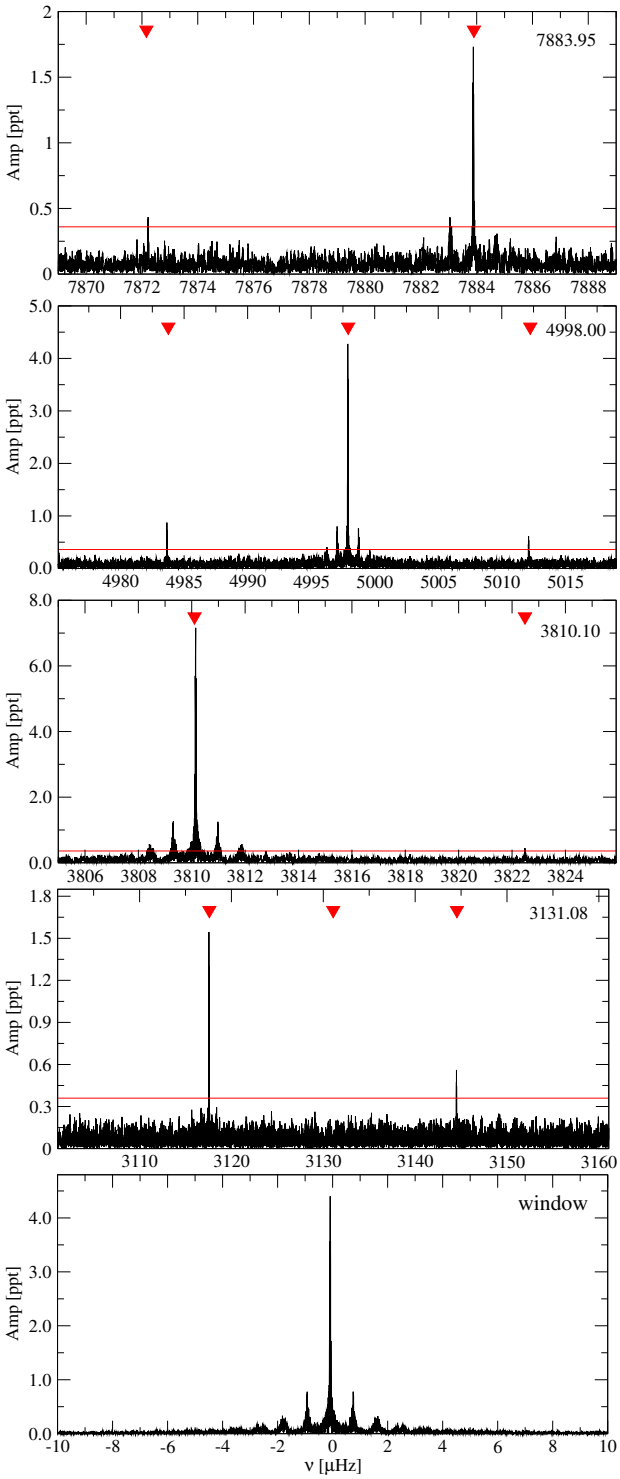

Figure 4. Detailed look at the FT for TIC 0055650407 around the detected multiplets centered around 7883.95, 4998,00, 3131,08 and 3117.60 μHz from top to bottom (see Table 6). The triangles indicate the position of the components, while the horizontal line indicates the amplitude detection limit. The bottom panel shows the corresponding spectral window for the data, with $\simeq 1\mu$Hz aliases.

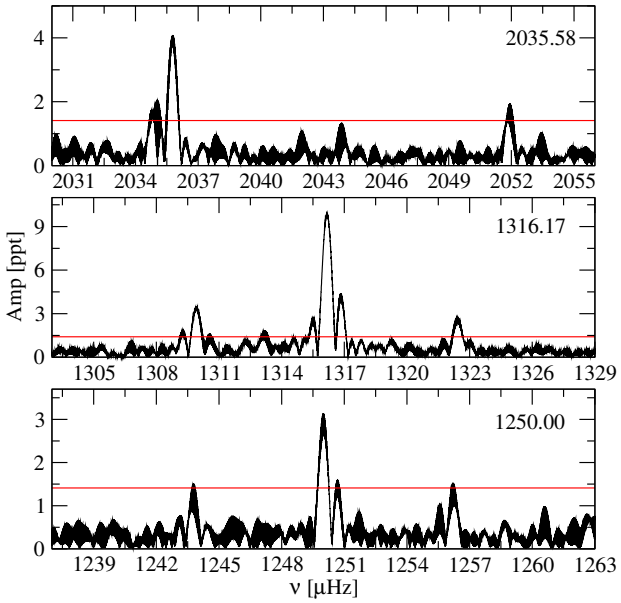

Figure 5. FT showing the multiplets for TIC 0149863849.

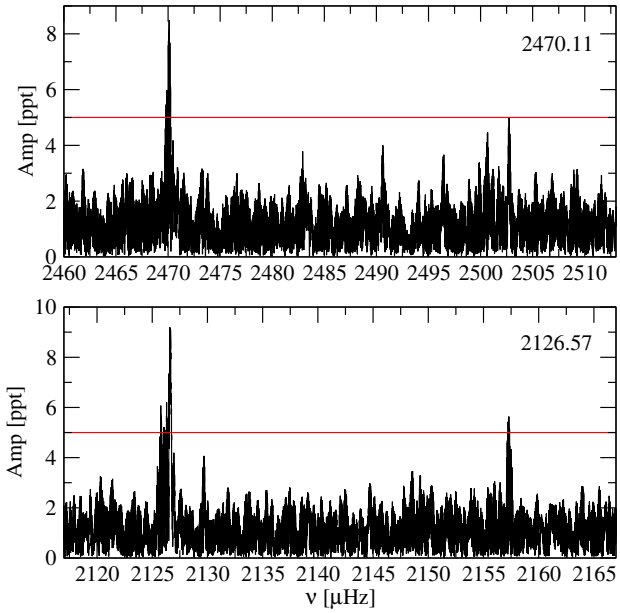

Figure 7. FT showing the doublets for TIC 0353727306.

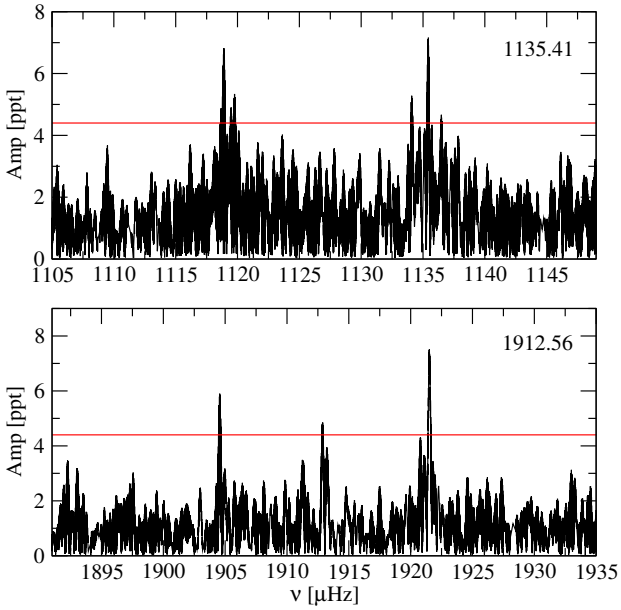

Figure 6. FT showing the doublet for TIC 0201860926.

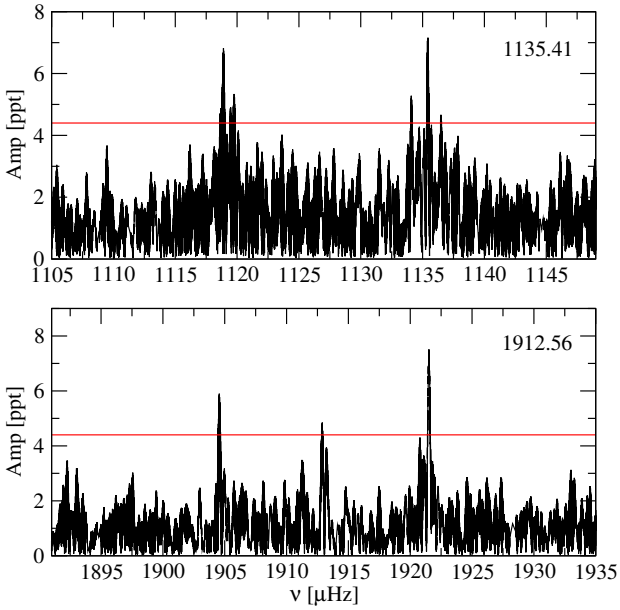

Figure 8. FT showing the multiplets for TIC 0201860926.

Figure 15 shows the comparison for the effective temperature values determined from Gaia photometry + parallax or spectroscopy (x axis) and asteroseismology (y axis). The uncertainties for the photometric or spectroscopic determinations are taken from Table 1. The internal uncertainties for the asteroseismological values are fixed by the resolution of the model grid to be 100 K, 200 K, and 300 K, for temperatures below 11 400 K, between 11 400 K and 11 800 K and above 11 800 K, respectively. The 16 objects with photometric or spectroscopic stellar masses below 0.49 $M_{\odot}$, which is the minimum mass of our C/O core model grid, are depicted as blue squares, while those with stellar masses above this value are depicted with black circles. As can be seen in Figure 15, the data cluster around the 1:1 correspondence line in red. Most of the outliers correspond to candidates for low-mass white dwarfs, with photometric effective temperatures above or below the blue and red edges of the instability strip, respectively (Tremblay et al. 2015; Hermes et al. 2017b).

TIC 0415337224 shows a photometric effective temperature of ~16,400 K, but the periods are long, which are

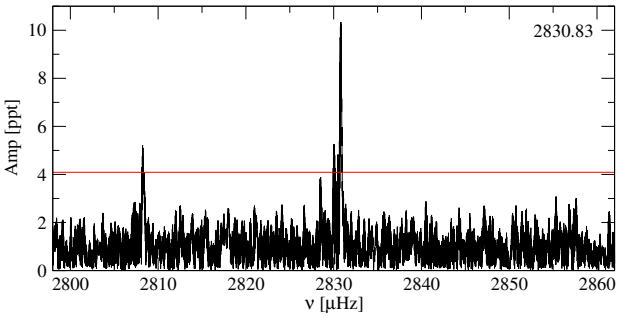

Figure 9. FT showing the doublet for TIC 0007675859

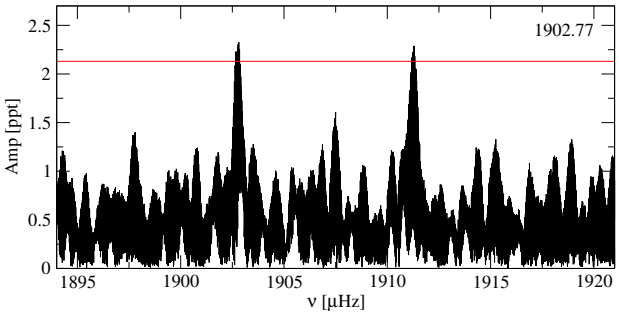

Figure 10. FT showing the doublet for TIC 0079353860.

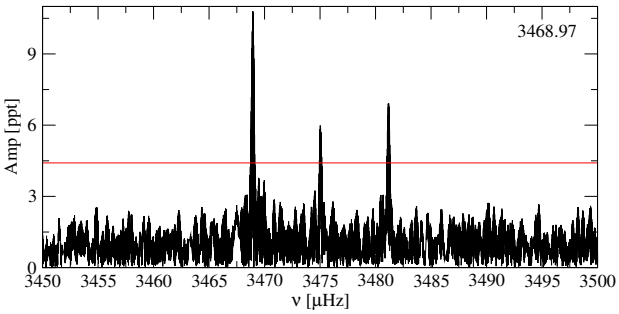

Figure 11. FT showing the triplet for TIC 0343296348.

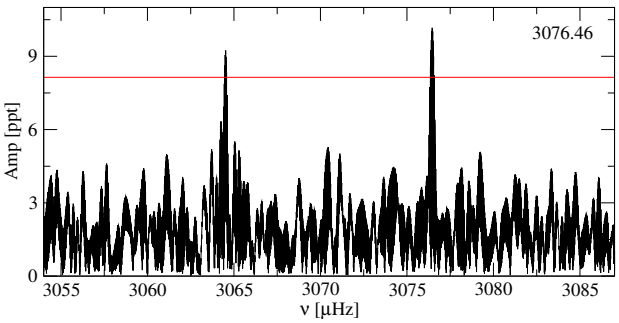

Figure 12. FT showing the doublet for TIC 0800126377.

characteristic of red edge pulsators (Mukadam et al. 2006). TIC 0103700861 shows the lowest effective photometric temperature of the sample, ~8500 K, with two periods around 500 and 700 s, characteristic of warm–like to cool pulsators,

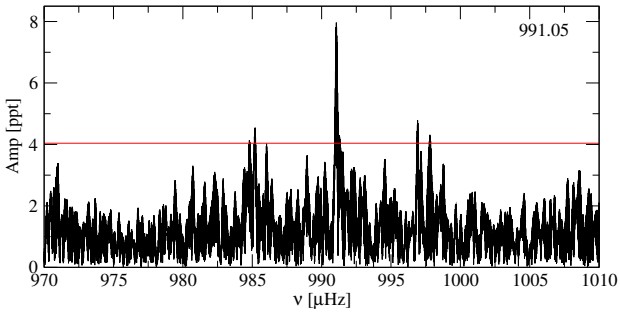

Figure 13. FT showing the triplet for TIC 1102242692.

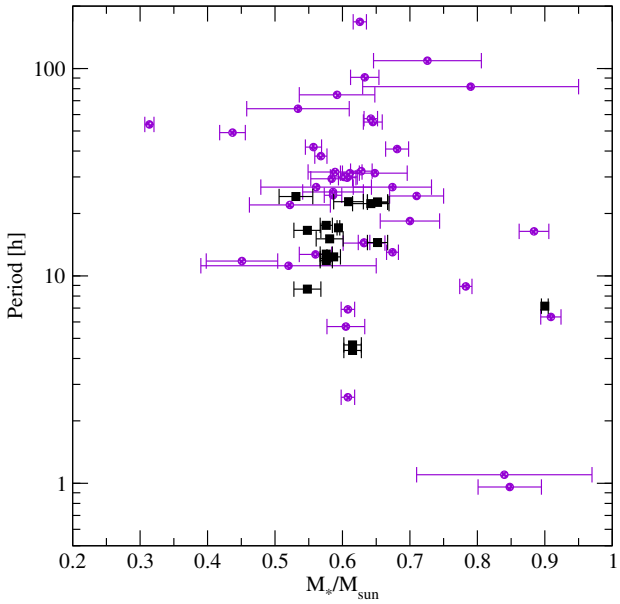

Figure 14. Rotation period obtained from asteroseismology as a function of stellar mass for DA white dwarfs (see Table 1). Purple dots correspond to values from the literature (Romero et al. 2022b; Fu et al. 2012; Bell et al. 2017; Su et al. 2013; Hermes et al. 2017b; Fu et al. 2019; Giammichele et al. 2016; Greiss et al. 2014; Kawaler 2015; Castanheira et al. 2013; Dolez, N. et al. 2006; Pech, D. & Vauclair, G. 2006; Bradley 2001; Pfeiffer et al. 1996; Kepler et al. 1995; Li et al. 2017), while black squares correspond to the data from Table 6. For the objects with more than one multiplet we include all rotation period determinations.

in agreement with the asteroseismological determination of the effective temperature. Both stars may have contaminated Gaia photometry.

In Figure 16 we compare the value of the stellar mass from photometry + Gaia parallax or spectroscopy (x axis) and from asteroseismology (y axis). We do not include objects with stellar masses below 0.49 $M_{\odot}$, which is the minimum mass of our C/O core model grid. Although the points are around the 1:1 correspondence line, there is a large scatter. The spread around the 1:1 correspondence line for stellar masses between 0.5 and 0.7 $M_{\odot}$ can be explained by means of the hydrogen envelope mass. For the same stellar mass, the

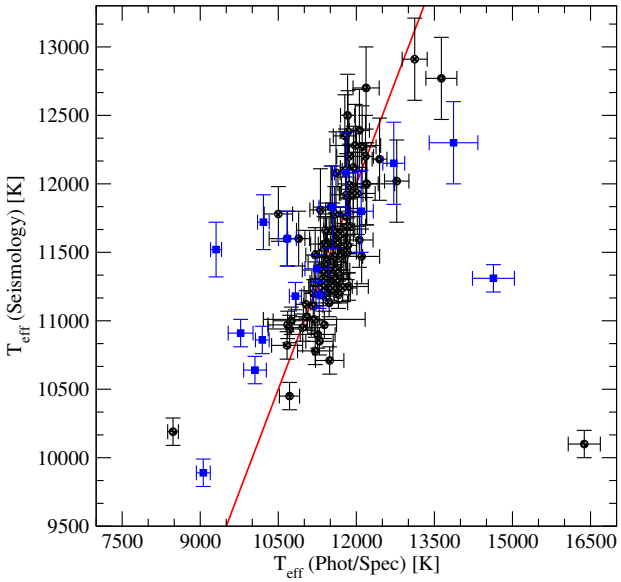

Figure 15. Comparison between the photometric or spectroscopic effective temperature (Table 1) and the asteroseismological effective temperature (Table 5). The red line indicates the 1:1 correspondence lines. Blue squares (black circles) correspond to objects with photometric or spectroscopic masses below (above) 0.49 $M_{\odot}$.

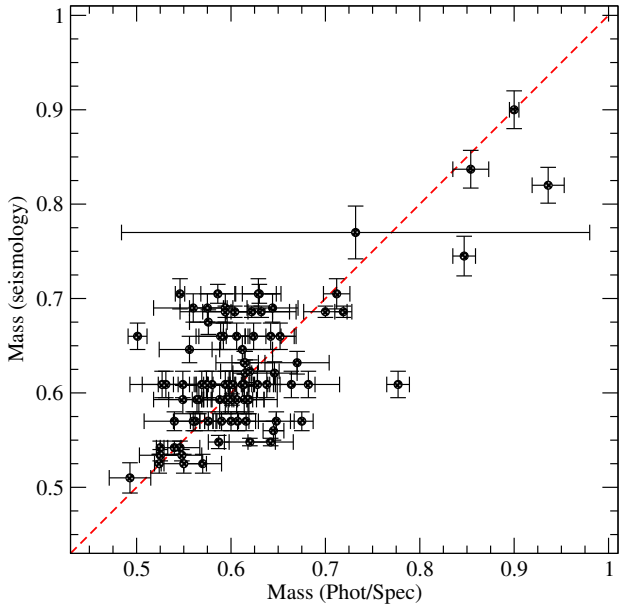

Figure 16. Comparison between the stellar mass obtained from photometry or spectroscopy (Table 1) and the asteroseismological fit (see Table 5). The red line indicates the 1:1 correspondence. Objects with photometric or spectroscopic masses below 0.49 $M_{\odot}$ are not included.

radius of the star is smaller the less hydrogen is left in the outer layers (Romero et al. 2019a), causing a degeneracy in the mass-radius relation. If only a canonical thick hydrogen envelope mass is considered to estimate the stellar mass from photometry and parallax, a thin envelope white dwarf will appear as a smaller and thus more massive star. The median of the stellar mass of the sample considered in Figure 16 is $\langle M_{\rm ph/sp} \rangle = 0.602\,{\rm M}_{\odot}$ for the values obtained by photometry or spectroscopy, while for the seismological mass, we obtain a value of $\langle M_{\rm seis} \rangle = 0.609\ {\rm M}_{\odot}$.

6.2. *Hydrogen envelope distribution*

The mass of the remaining hydrogen content in the envelope of a DA white dwarf star can be estimated almost exclusively by asteroseismology. For the sample studied in this work, the value of the hydrogen envelope mass is listed in column 3 of Table 5. As can be seen from Table 4, the maximum mass of the hydrogen envelope that can be present on top of a DA white dwarf depends on the stellar mass, being thinner for higher masses (Romero et al. 2012, 2019a). Thus, the maximum hydrogen envelope mass canonical value) ranges from $10^{-3.5}{\rm M}_{*}$ for 0.49 $\rm M_{\odot}$ to $\sim 10^{-6}{\rm M}_{*} \sim 1\ {\rm M}_{\odot}$.

The distribution of hydrogen envelope thickness for the sample of 103 ZZ Cetis observed by TESS is shown in the upper panel of Fig. 17. The middle and bottom panels show the distribution for the canonical envelopes, those with the thickest envelope allowed by single stellar evolution, and the thin envelopes, respectively. Dashed bars correspond to the 51 objects with more than two observed periods, while the full symbol considers the hole sample. The hydrogen envelope thickness distribution shows a distinctive maximum for $-\log(M_H/M_*)$ between -5 and -4, with contributions from canonical envelopes from the models with stellar masses above ~0.6 $\rm M_{\odot}$ and non-canonical envelopes for the low-mass models, as seen in previous works (Romero et al. 2012, 2013, 2019b). Contributions to canonical envelopes between $-\log(M_H/M_*)$ -5 and -6 come from massive sequences, with masses above 0.84 $\rm M_{\odot}$, as can be seen from the middle panel in figure 17. The gap between $-\log(M_H/M_*)-7$ and -8, previously noticed by Romero et al. (2012) using 44 ZZ Cetis, does not seem to be significant for our sample, which could be related to the larger number of objects considered in this work.

From our sample of 103 objects we found that, 65 per cent show hydrogen envelopes thicker than $10^{-6}{\rm M}_{*}$, or 75 per cent if we only consider objects showing more than 2 periods. This result is in agreement with those presented by Clemens et al. (2017) from a sample of 16 hot ZZ Ceti stars. They found that the best-matching models, taken from the model grid presented in Romero et al. (2012), have hydrogen layer masses values near the canonically thick limit calculated from nuclear burning.

The spectral evolution presented by Tremblay & Bergeron (2008), and more recently by Ourique et al. (2019); Cunningham et al. (2020), where the ratio of non–DA to DA white dwarfs increases a factor of five for effective temperatures around 12 500 K. The most likely explanation is the occur-

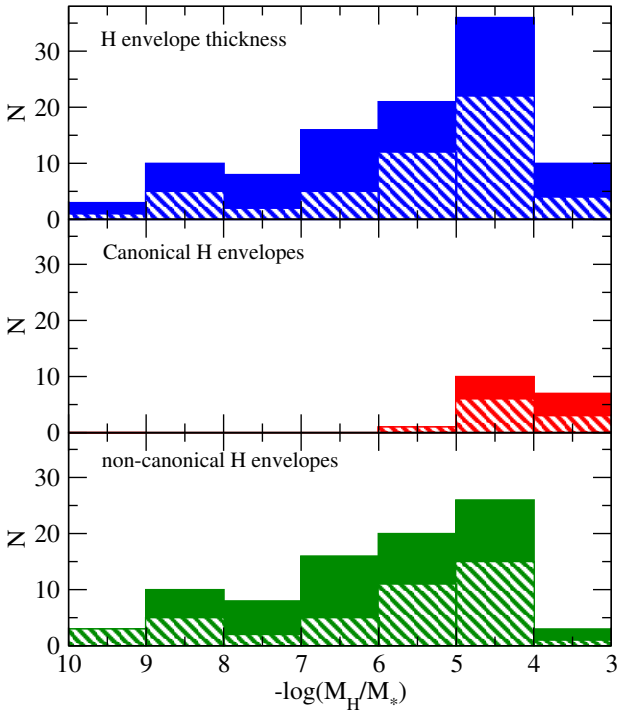

Figure 17. Upper panel: histogram showing the hydrogen envelope thickness distribution for the 105 objects. Middle panel: histogram for models with canonical values of the hydrogen envelope thickness, as predicted by stellar evolution theory for each mass. Lower panel: histogram for models with non-canonical values of the hydrogen envelope thickness We consider only the best-fit model solutions for each star. In addition, with dashed bars, we show the results corresponding to a sample composed only with stars having three or more modes in their spectrum.

rence of convective mixing of the hydrogen layer into the more massive helium layer below. In order to reproduce this result (Ourique et al. 2019) found that a fraction around 10–17 per cent of DA white dwarf stars should have hydrogen envelopes thinner than $M_H/M_* = 10^{-8}$. From our sample, we found that 12.5 per cent of the 103 ZZ Cetis are fitted by models with hydrogen envelopes thinner than $10^{-8}M_*$, or 11.8 per cent if we consider only the objects presenting more than 2 detected periods.

6.3. *Weighed mean period*

From the observed period spectrum of the 103 variable DAV stars, we can compute the weighted mean period (WMP) as:

$$\mathrm{WMP} = \frac{\sum_i P_i A_i}{\sum_i A_i}, \qquad (4)$$

where P_1 is the observed period and A_i its amplitude. Mukadam et al. (2006), using the available sample of known ZZ Cetis at the time and atmosphere parameters obtained from spectroscopy, found a relation between the WMP and the effective temperature. According to their results, the value of

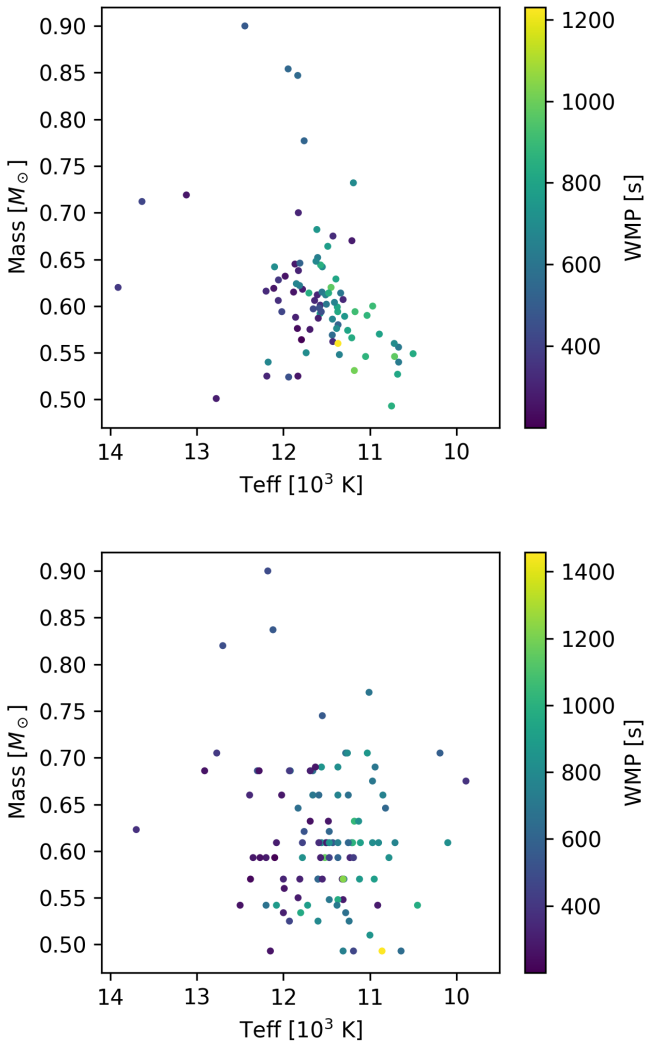

Figure 18. Value of the weighted mean period (WMP) as a function of photometric or spectroscopic (top panel) and seismological (bottom panel) stellar mass and effective temperature. The value of the WMP is shown in the color scale.

the WMP increases for lower effective temperatures. In the following, we revisit this relation using the sample of 103 DAVs discovered from TESS data.

The WMP as a function of stellar mass and effective temperature is depicted in Figure 18, for values obtained from photometry or spectroscopy (top panel) and the asteroseismological fit (bottom panel). The value of the WMP is on a color scale. We consider objects with photometric or spectroscopic stellar masses larger than 0.49 $M_\odot$ and effective temperatures between 10,000 and 14,000 K. From these figures, we found a dependence of the WMP on the effective temperature, which is shorter for higher temperatures, in agreement with the results presented in Mukadam et al. (2006). The value of the Pearson coefficient is −0.51 for the photometric

or spectroscopic effective temperature determinations, indicating a moderate correlation of the WMP with this parameter. In the case of the effective temperature obtained from the asteroseimological fits, the Pearson coefficient is −0.57, also indicating a moderate correlation. Assuming a linear dependence of the WMP with the effective temperature, we obtain the following relations.

$$\mathrm{WMP}(s) = -0.197 \times T_{\mathrm{eff}}(K) + 2876 \quad (5)$$

for photometric or spectroscopic effective temperatures, and

$$\mathrm{WMP}(s) = -0.267 \times T_{\mathrm{eff}}(K) + 3680 \quad (6)$$

for effective temperature obtained from asteroseismology, with T_{eff} in K and the WMP in seconds. Finally, there is no clear dependence of the WMP on stellar mass.

The WMP is usually dominated by the period with the highest amplitude, especially when the amplitude differences are large. However, if the period amplitudes are similar, the WMP can differ from the highest-amplitude period (HAP). Figure 19 shows the comparison between the WMP (x-axis) and the HAP (y-axis), for objects with more than one observed period. As expected, the data values are close to the 1:1 correspondence line in red, but a dispersion is observed from the plot. For periods around ∼700 s, the WMP value tends to be higher than the HAP value, while for periods longer than ∼700 s the WMP is shorter than the HAP. The Pearson coefficient is 0.85, indicating a strong correlation.

In Figure 20 we depict the value of the HAP as a function of effective temperature and stellar mass obtained from photometry or spectroscopy and asteroseismology in the top and bottom panels, respectively. The value of the HAP is represented on the color scale. In the figure, we note that the value of the HAP also increases with decreasing effective temperatures, following the same trend as the WMP. The Pearson coefficient is −0.52 and −0.57, when we consider the effective temperatures from photometry or spectroscopy and asteroseismology, respectively, indicating a moderate correlation of the HAP with this parameter.

There is also a dependence with stellar mass for effective temperatures higher than ∼12,000 K, where the HAP values increase with stellar mass. However, given that there are few objects with stellar masses larger than ∼0.7 $M_{\odot}$, this dependence is not well grounded.

7. SUMMARY

In the first five years, TESS has already proven to be a powerful tool in discovering new pulsating white dwarfs. Although it is a small telescope with low spatial resolution, its excellent time span has allowed not only the discovery of more than 100 new pulsating white dwarfs but also the detection of multiplets in many of them.

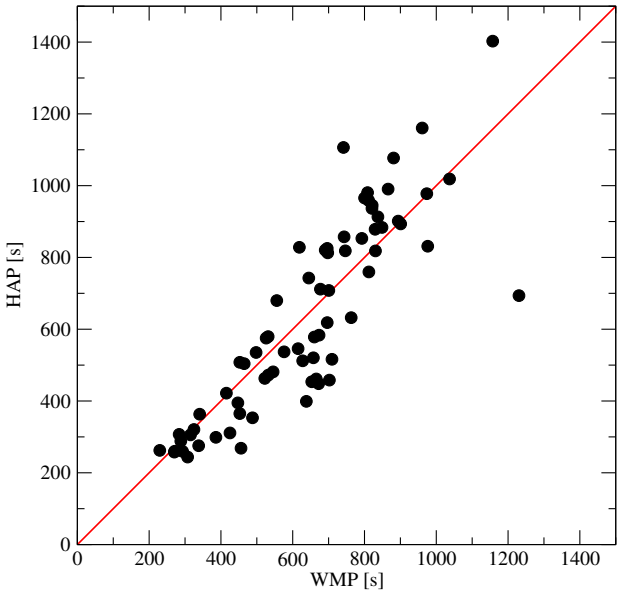

Figure 19. Comparison between the values of the weighed mean period (WMP) and the highest amplitude period (HAP). Objects with only one period are not included. The red line indicate the 1:1 relation.

In this work, we present the discovery of 32 new pulsating DA white dwarf stars, based on observations of the TESS mission from Sector 40 to Sector 69. In addition, we revisited 21 ZZ Cetis reported by Romero et al. (2022b) that present differences in their period spectra, after observations from Cycles 4 and 5 were considered. The complete sample of pulsating DA white dwarfs discovered using TESS observations is now 103 objects. For each object, we performed an asteroseismological study and determined the main structure parameters such as stellar mass, effective temperature, and hydrogen envelope mass. In cases where only one or two periods were detected, we use the photometric or spectroscopic observations as an additional constraint to the fit.

We detected a component of rotational splitting for 9 objects, with rotation periods from 4 h to 1 d, in line with the observed rotation period distribution obtained from asteroseismology for other known DA white dwarf stars. For four objects, we detected more than one multiplet that could open the opportunity to study radial differential rotation. The median for the rotation period for the 9 objects reported in this work is 13.6 h almost three times smaller than the mean rotation period for the 41 ZZ Cetis obtained from the literature.

The median value for the stellar mass for the sample of ZZ Ceti from TESS from photometry and/or spectroscopy and seismology is $\langle M_{\mathrm{ph/sp}} \rangle$ = 0.602 $\mathrm{M}_{\odot}$ and $\langle M_{\mathrm{seis}} \rangle$ = 0.609 $\mathrm{M}_{\odot}$, respectively. These values are in line with the mean stellar mass of 351 known ZZ Ceti stars of $\langle M_{\mathrm{seis}} \rangle$ = 0.644 ± 0.034$M_{\odot}$ (Romero et al. 2022b). The distribution of the hydrogen envelope mass shows a distinctive peak be-

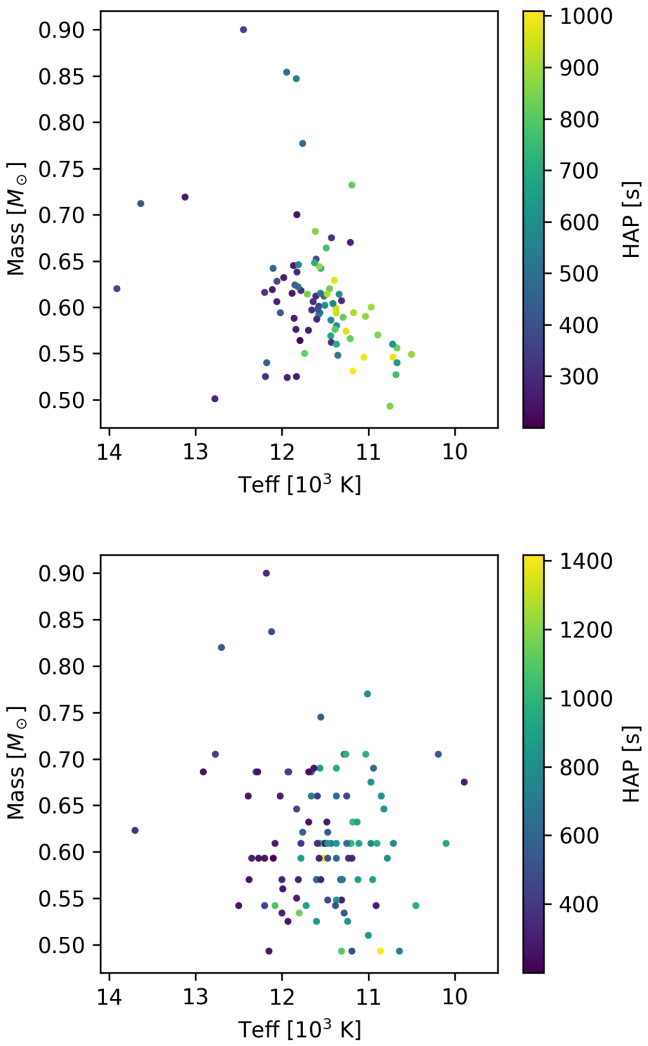

Figure 20. Value of the highest amplitude period (HAP) as a function of photometric or spectroscopic (top panel) and seismological (bottom panel) stellar mass and effective temperature. The value of the HAP is shown in the color scale.

tween $-\log(M_H/M_*)$ between -5 and -4, in agreement with previous works, showing that, for $\sim$ 65 per cent DA white dwarf stars, the mass of the hydrogen layer is determine by residual burning at the beginning of the cooling curve.

Finally, we revisit the relation between the weighted mean period and the effective temperature. We found a moderate correlation for both the photometric or spectroscopic and the seismological effective temperatures with the WMP value. We did not find a strong dependence on the stellar mass.

The authors thank Zsófia Sódorné Bognár and Keaton Bell for the comments and suggestions on the manuscript. This study was financed in part by the Coordenação de Aperfeiçoamento de Pessoal de Nível Superior - Brasil (CAPES) - Finance Code 001, Conselho Nacional de Desenvolvimento Científico e Tecnológico - Brasil (CNPq), and Fundação de Amparo à Pesquisa do Rio Grande do Sul (FAPERGS) - Brazil. This paper includes data collected with the TESS mission, obtained from the MAST data archive at the Space Telescope Science Institute (STScI). Funding for the TESS mission is provided by the NASA Explorer Program. All the TESS data used in this article can be found in MAST (Team 2021a,b,c,d). This work has used data from the Gaia mission of the European Space Agency (ESA) (https://www.cosmos.esa.int/gaia), processed by the Gaia Data Processing and Analysis Consortium (DPAC, https://www.cosmos.esa.int/web/gaia/dpac/consortium). Funding for the DPAC has been provided by national institutions, in particular the institutions participating in the Gaia Multilateral Agreement. Most of the calculations were performed at the Texas Advanced Computing Center, located at the University of Texas in Austin. This research has made extensive use of NASA's Astrophysics Data System Bibliographic Service (ADS), SIMBAD (Wenger et al. 2000), MAST, and the Montreal White Dwarf Database (Dufour et al. 2017).

Software: We used ASTROPY (https://www.astropy.org/) Astropy Collaboration et al. (2013, 2018, 2022), TESS-LS (https://github.com/ipelisoli/TESS-LS), TESS_LOCALIZE Higgins & Bell (2023) (https://github.com/Higgins00/TESS-Localizer), LIGHTKURVE (https://docs.lightkurve.org/) and PYRIOD (https://github.com/keatonb/Pyriod).

REFERENCES

Althaus, L. G., Córsico, A. H., Bischoff-Kim, A., et al. 2010, ApJ, 717, 897, doi: 10.1088/0004-637X/717/2/897

Althaus, L. G., Miller Bertolami, M. M., Córsico, A. H., García-Berro, E., & Gil-Pons, P. 2005, A&A, 440, L1, doi: 10.1051/0004-6361:200500159

Astropy Collaboration, Robitaille, T. P., Tollerud, E. J., et al. 2013, A&A, 558, A33, doi: 10.1051/0004-6361/201322068

Astropy Collaboration, Price-Whelan, A. M., Sipőcz, B. M., et al. 2018, AJ, 156, 123, doi: 10.3847/1538-3881/aabc4f

Astropy Collaboration, Price-Whelan, A. M., Lim, P. L., et al. 2022, ApJ, 935, 167, doi: 10.3847/1538-4357/ac7c74

Bell, K. J., Hermes, J. J., Vanderbosch, Z., et al. 2017, The Astrophysical Journal, 851, 24, doi: 10.3847/1538-4357/aa9702

Bergeron, P., Dufour, P., Fontaine, G., et al. 2019, ApJ, 876, 67, doi: 10.3847/1538-4357/ab153a

Bergeron, P., Ruiz, M. T., & Leggett, S. K. 1997, ApJS, 108, 339, doi: 10.1086/312955

Bischoff-Kim, A., Østensen, R. H., Hermes, J. J., & Provencal, J. L. 2014, ApJ, 794, 39, doi: 10.1088/0004-637X/794/1/39

Bognar, Z., & Sodor, A. 2016, Information Bulletin on Variable Stars, 6184, 1. https://arxiv.org/abs/1610.07470

Bognár, Z., Sódor, Á., Clark, I. R., & Kawaler, S. D. 2023, A&A, 674, A204, doi: 10.1051/0004-6361/202245177

Bognár, Z., Kawaler, S. D., Bell, K. J., et al. 2020, A&A, 638, A82, doi: 10.1051/0004-6361/202037470

Bond, H. E., Bergeron, P., & Bédard, A. 2017, ApJ, 848, 16, doi: 10.3847/1538-4357/aa8a63

Bradley, P. A. 2001, The Astrophysical Journal, 552, 326, doi: 10.1086/320454

Brassard, P., Fontaine, G., & Wesemael, F. 1995, ApJS, 96, 545, doi: 10.1086/192128

Brickhill, A. J. 1991, MNRAS, 251, 673, doi: 10.1093/mnras/251.4.673

Castanheira, B. G., Kepler, S. O., Kleinman, S. J., Nitta, A., & Fraga, L. 2013, MNRAS, 430, 50, doi: 10.1093/mnras/sts474

Chambers, K. C., Magnier, E. A., Metcalfe, N., et al. 2016, arXiv e-prints, arXiv:1612.05560. https://arxiv.org/abs/1612.05560

Clemens, J. C. 1993, Baltic Astronomy, 2, 407, doi: 10.1515/astro-1993-3-410

Clemens, J. C., O'Brien, P. C., Dunlap, B. H., & Hermes, J. J. 2017, in Astronomical Society of the Pacific Conference Series, Vol. 509, 20th European White Dwarf Workshop, ed. P. E. Tremblay, B. Gaensicke, & T. Marsh, 255, doi: 10.48550/arXiv.1611.02579

Córsico, A. H., & Althaus, L. G. 2006, A&A, 454, 863, doi: 10.1051/0004-6361:20054199

Córsico, A. H., Althaus, L. G., Miller Bertolami, M. M., & Kepler, S. O. 2019, A&A Rv, 27, 7, doi: 10.1007/s00159-019-0118-4

Córsico, A. H., Romero, A. D., Althaus, L. G., & Hermes, J. J. 2012, A&A, 547, A96, doi: 10.1051/0004-6361/201220114

Cowling, T. G., & Newing, R. A. 1949, ApJ, 109, 149, doi: 10.1086/145114

Cunningham, T., Tremblay, P.-E., Gentile Fusillo, N. P., Hollands, M., & Cukanovaite, E. 2020, MNRAS, 492, 3540, doi: 10.1093/mnras/stz3638

Da Rosa, G. O., Kepler, S. O., Soethe, L. T. T., Romero, A. D., & Bell, K. J. 2024, ApJ, submited

Dolez, N., & Vauclair, G. 1981, A&A, 102, 375

Dolez, N., Vauclair, G., Kleinman, S. J., et al. 2006, A&A, 446, 237, doi: 10.1051/0004-6361:20053149

Dufour, P., Blouin, S., Coutu, S., et al. 2017, in Astronomical Society of the Pacific Conference Series, Vol. 509, 20th European White Dwarf Workshop, ed. P. E. Tremblay, B. Gaensicke, & T. Marsh, 3, doi: 10.48550/arXiv.1610.00986

Eastman, J., Siverd, R., & Gaudi, B. S. 2010, PASP, 122, 935, doi: 10.1086/655938

Eisenstein, D. J., Liebert, J., Harris, H. C., et al. 2006, ApJS, 167, 40, doi: 10.1086/507110

Fu, J.-N., Dolez, N., Vauclair, G., et al. 2012, Monthly Notices of the Royal Astronomical Society, 429, 1585, doi: 10.1093/mnras/sts438

Fu, J.-N., Vauclair, G., Su, J., et al. 2019, Monthly Notices of the Royal Astronomical Society, 486, 3560, doi: 10.1093/mnras/stz1088

Gentile Fusillo, N. P., Tremblay, P.-E., Gänsicke, B. T., et al. 2019, MNRAS, 482, 4570, doi: 10.1093/mnras/sty3016

Gentile Fusillo, N. P., Tremblay, P. E., Cukanovaite, E., et al. 2021, MNRAS, 508, 3877, doi: 10.1093/mnras/stab2672

Giammichele, N., Fontaine, G., Brassard, P., & Charpinet, S. 2016, The Astrophysical Journal Supplement Series, 223, 10, doi: 10.3847/0067-0049/223/1/10

Gianninas, A., Bergeron, P., & Ruiz, M. T. 2011, ApJ, 743, 138, doi: 10.1088/0004-637X/743/2/138

Goldreich, P., & Wu, Y. 1999, ApJ, 511, 904, doi: 10.1086/306705

Greiss, S., Gänsicke, B. T., Hermes, J. J., et al. 2014, Monthly Notices of the Royal Astronomical Society, 438, 3086, doi: 10.1093/mnras/stt2420

Guidry, J. A., Vanderbosch, Z. P., Hermes, J. J., et al. 2021, ApJ, 912, 125, doi: 10.3847/1538-4357/abee68

Hermes, J. J., Gänsicke, B. T., Kawaler, S. D., et al. 2017, ApJS, 232, 23, doi: 10.3847/1538-4365/aa8bb5

—. 2017b, ApJS, 232, 23, doi: 10.3847/1538-4365/aa8bb5

Higgins, M. E., & Bell, K. J. 2023, AJ, 165, 141, doi: 10.3847/1538-3881/acb20c

Istrate, A. G., Marchant, P., Tauris, T. M., et al. 2016, A&A, 595, A35, doi: 10.1051/0004-6361/201628874

Istrate, A. G., Tauris, T. M., & Langer, N. 2014, A&A, 571, A45, doi: 10.1051/0004-6361/201424680

Jenkins, J. M., Twicken, J. D., McCauliff, S., et al. 2016, in Society of Photo-Optical Instrumentation Engineers (SPIE) Conference Series, Vol. 9913, Software and Cyberinfrastructure for Astronomy IV, ed. G. Chiozzi & J. C. Guzman, 99133E, doi: 10.1117/12.2233418

Kawaler, S. D. 2004, in Stellar Rotation, ed. A. Maeder & P. Eenens, Vol. 215, 561

Kawaler, S. D. 2015, in Astronomical Society of the Pacific Conference Series, Vol. 493, 19th European Workshop on White Dwarfs, ed. P. Dufour, P. Bergeron, & G. Fontaine, 65, doi: 10.48550/arXiv.1410.6934

Kawka, A., & Vennes, S. 2012, MNRAS, 425, 1394, doi: 10.1111/j.1365-2966.2012.21574.x

Kepler, S. O. 1993, Baltic Astronomy, 2, 515, doi: 10.1515/astro-1993-3-425

—. 2007, Communications in Asteroseismology, 150, 221, doi: 10.1553/cia150s221

Kepler, S. O., Koester, D., Pelisoli, I., Romero, A. D., & Ourique, G. 2021, MNRAS, 507, 4646, doi: 10.1093/mnras/stab2411

Kepler, S. O., & Romero, A. D. 2017, in European Physical Journal Web of Conferences, Vol. 152, European Physical Journal Web of Conferences, 01011, doi: 10.1051/epjconf/201715201011

Kepler, S. O., Giovannini, O., Wood, M. A., et al. 1995, ApJ, 447, 874, doi: 10.1086/175924

Kepler, S. O., Pelisoli, I., Koester, D., et al. 2019, MNRAS, 486, 2169, doi: 10.1093/mnras/stz960

Kilic, M., Bergeron, P., Kosakowski, A., et al. 2020, ApJ, 898, 84, doi: 10.3847/1538-4357/ab9b8d

Kilic, M., Stanek, K. Z., & Pinsonneault, M. H. 2007, ApJ, 671, 761, doi: 10.1086/522228

Kleinman, S. J., Kepler, S. O., Koester, D., et al. 2013, ApJS, 204, 5, doi: 10.1088/0067-0049/204/1/5

Landolt, A. U. 1968, ApJ, 153, 151, doi: 10.1086/149645

Lasker, B. M., & Hesser, J. E. 1971, ApJL, 163, L89, doi: 10.1086/180673

Ledoux, P. 1951, ApJ, 114, 373, doi: 10.1086/145477

Li, C., Fu, J., Fox-Machado, L., Su, J., & Chen, F. 2017, NewA, 55, 48, doi: 10.1016/j.newast.2017.03.003

Limoges, M. M., Lépine, S., & Bergeron, P. 2013, AJ, 145, 136, doi: 10.1088/0004-6256/145/5/136

Montgomery, M. H., Hermes, J. J., Winget, D. E., Dunlap, B. H., & Bell, K. J. 2020, ApJ, 890, 11, doi: 10.3847/1538-4357/ab6a0e

Mukadam, A. S., Montgomery, M. H., Winget, D. E., Kepler, S. O., & Clemens, J. C. 2006, ApJ, 640, 956, doi: 10.1086/500289

O'Brien, M. W., Tremblay, P. E., Gentile Fusillo, N. P., et al. 2023, MNRAS, 518, 3055, doi: 10.1093/mnras/stac3303

Ourique, G., Kepler, S. O., Romero, A. D., Klippel, T. S., & Koester, D. 2020, MNRAS, 492, 5003, doi: 10.1093/mnras/staa120

Ourique, G., Romero, A. D., Kepler, S. O., Koester, D., & Amaral, L. A. 2019, MNRAS, 482, 649, doi: 10.1093/mnras/sty2751

Pech, D., & Vauclair, G. 2006, A&A, 453, 219, doi: 10.1051/0004-6361:20054370

Pelisoli, I., & Vos, J. 2019, MNRAS, 488, 2892, doi: 10.1093/mnras/stz1876

Pfeiffer, B., Vauclair, G., Dolez, N., et al. 1996, A&A, 314, 182

Raddi, R., Gentile Fusillo, N. P., Pala, A. F., et al. 2017, MNRAS, 472, 4173, doi: 10.1093/mnras/stx2243

Renedo, I., Althaus, L. G., Miller Bertolami, M. M., et al. 2010, ApJ, 717, 183, doi: 10.1088/0004-637X/717/1/183

Ricker, G. R., Winn, J. N., Vanderspek, R., et al. 2014, in Society of Photo-Optical Instrumentation Engineers (SPIE) Conference Series, Vol. 9143, Space Telescopes and Instrumentation 2014: Optical, Infrared, and Millimeter Wave, ed. J. Oschmann, Jacobus M., M. Clampin, G. G. Fazio, & H. A. MacEwen, 914320, doi: 10.1117/12.2063489

Romero, A. D., Campos, F., & Kepler, S. O. 2015, MNRAS, 450, 3708, doi: 10.1093/mnras/stv848

Romero, A. D., Córsico, A. H., Althaus, L. G., et al. 2012, MNRAS, 420, 1462, doi: 10.1111/j.1365-2966.2011.20134.x

Romero, A. D., Kepler, S. O., Córsico, A. H., Althaus, L. G., & Fraga, L. 2013, ApJ, 779, 58, doi: 10.1088/0004-637X/779/1/58

Romero, A. D., Kepler, S. O., Joyce, S. R. G., Lauffer, G. R., & Córsico, A. H. 2019a, MNRAS, 484, 2711, doi: 10.1093/mnras/stz160

Romero, A. D., Lauffer, G. R., Istrate, A. G., & Parsons, S. G. 2022a, MNRAS, 510, 858, doi: 10.1093/mnras/stab3487

Romero, A. D., Córsico, A. H., Castanheira, B. G., et al. 2017, ApJ, 851, 60, doi: 10.3847/1538-4357/aa9899

Romero, A. D., Amaral, L. A., Klippel, T., et al. 2019b, MNRAS, 490, 1803, doi: 10.1093/mnras/stz2571

Romero, A. D., Kepler, S. O., Hermes, J. J., et al. 2022b, MNRAS, 511, 1574, doi: 10.1093/mnras/stac093

Rowan, D. M., Tucker, M. A., Shappee, B. J., & Hermes, J. J. 2019, MNRAS, 486, 4574, doi: 10.1093/mnras/stz1116

Sturrock, P. A., & Scargle, J. D. 2010, ApJ, 718, 527, doi: 10.1088/0004-637X/718/1/527

Su, J., Fu, J., Lin, G., et al. 2017, ApJ, 847, 34, doi: 10.3847/1538-4357/aa88a8

Su, J., Li, Y., Fu, J.-N., & Li, C. 2013, Monthly Notices of the Royal Astronomical Society, 437, 2566, doi: 10.1093/mnras/stt2069

Team, M. 2021a, TESS "Fast" Light Curves - All Sectors, STScI/MAST, doi: 10.17909/T9-ST5G-3177

—. 2021b, TESS "Fast" Target Pixel Files - All Sectors, STScI/MAST, doi: 10.17909/T9-TCN7-7G94

—. 2021c, TESS Light Curves - All Sectors, STScI/MAST, doi: 10.17909/T9-NMC8-F686

—. 2021d, TESS Target Pixel Files - All Sectors, STScI/MAST, doi: 10.17909/T9-YK4W-ZC73

Tremblay, P. E., & Bergeron, P. 2008, ApJ, 672, 1144, doi: 10.1086/524134

Tremblay, P. E., Bergeron, P., & Gianninas, A. 2011, ApJ, 730, 128, doi: 10.1088/0004-637X/730/2/128

Tremblay, P. E., Gianninas, A., Kilic, M., et al. 2015, ApJ, 809, 148, doi: 10.1088/0004-637X/809/2/148

Tremblay, P. E., Ludwig, H. G., Steffen, M., & Freytag, B. 2013, A&A, 559, A104, doi: 10.1051/0004-6361/201322318

Tremblay, P. E., Hollands, M. A., Gentile Fusillo, N. P., et al. 2020, MNRAS, 497, 130, doi: 10.1093/mnras/staa1892

Van Horn, H. M. 2015, Unlocking the Secrets of White Dwarf Stars, doi: 10.1007/978-3-319-09369-7

VanderPlas, J. T. 2018, ApJS, 236, 16, doi: 10.3847/1538-4365/aab766

Vincent, O., Bergeron, P., & Lafrenière, D. 2020, AJ, 160, 252, doi: 10.3847/1538-3881/abbe20

Vio, R., Andreani, P., Biggs, A., & Hayatsu, N. 2019, A&A, 627, A103, doi: 10.1051/0004-6361/201834854

Wang, K., Zhang, X., & Dai, M. 2020, ApJ, 888, 49, doi: 10.3847/1538-4357/ab584c

Wenger, M., Ochsenbein, F., Egret, D., et al. 2000, A&AS, 143, 9, doi: 10.1051/aas:2000332

Winget, D. E., van Horn, H. M., Tassoul, M., et al. 1982, ApJL, 252, L65, doi: 10.1086/183721

Winget, D. E., Nather, R. E., Clemens, J. C., et al. 1991, ApJ, 378, 326, doi: 10.1086/170434

—. 1994, ApJ, 430, 839, doi: 10.1086/174455

Zong, W., Charpinet, S., Vauclair, G., Giammichele, N., & Van Grootel, V. 2016, A&A, 585, A22, doi: 10.1051/0004-6361/201526300

APPENDIX

Fourier Transforms for the new 32 ZZ Cetis studied in this work considering the concatenated data of all observed sectors.

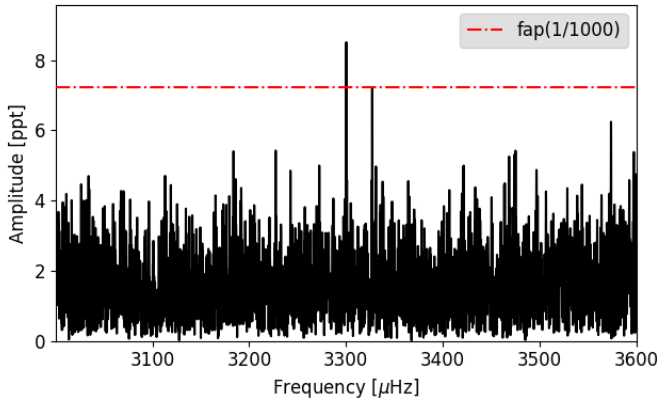

Figure 21. Fourier Transform for TIC 0000116746.

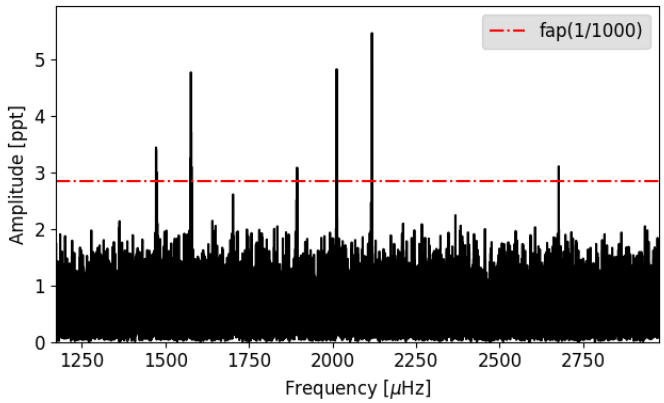

Figure 22. Fourier Transform for TIC 0014448610.

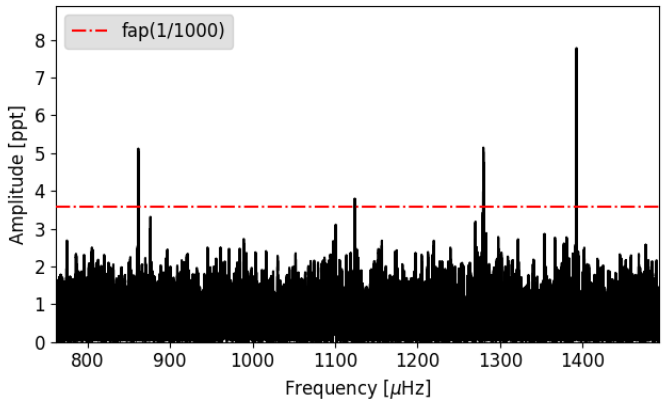

Figure 23. Fourier Transform for TIC 0030545382.

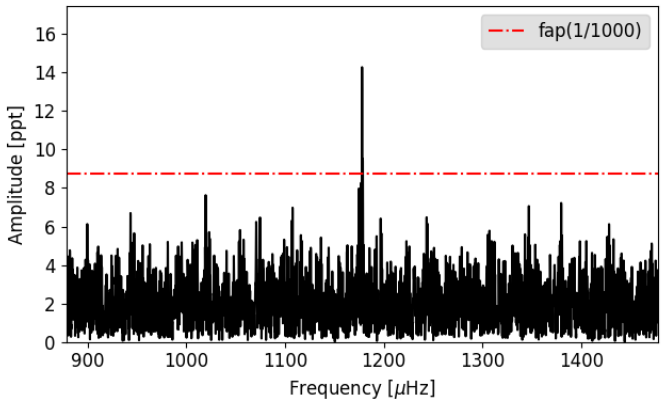

Figure 24. Fourier Transform for TIC 0072517198.

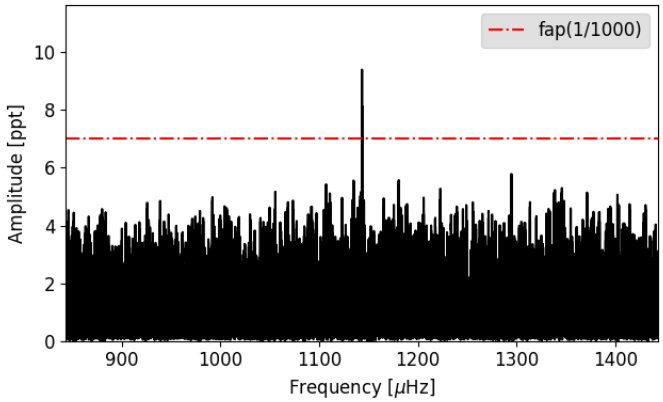

Figure 25. Fourier Transform for TIC 0081848974.

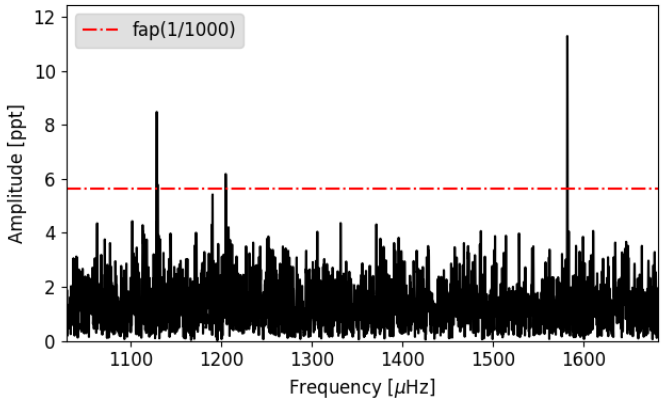

Figure 26. Fourier Transform for TIC 0088046487.

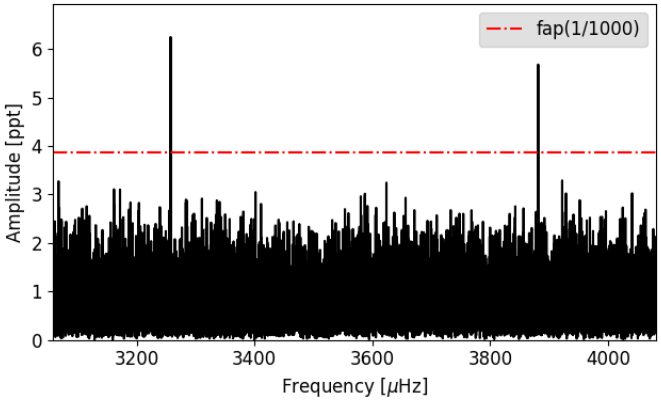

Figure 27. Fourier Transform for TIC 0094748632.

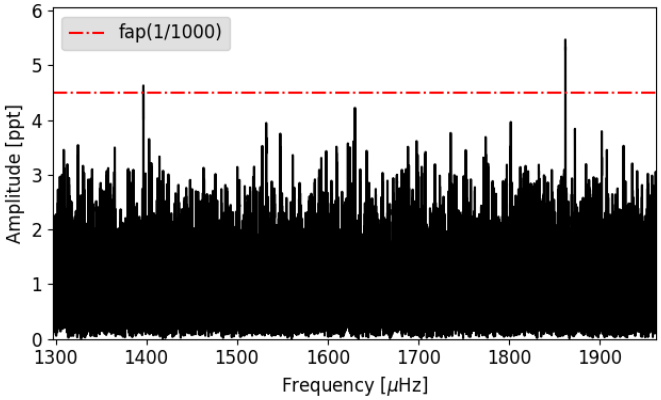

Figure 28. Fourier Transform for TIC 0103700861.

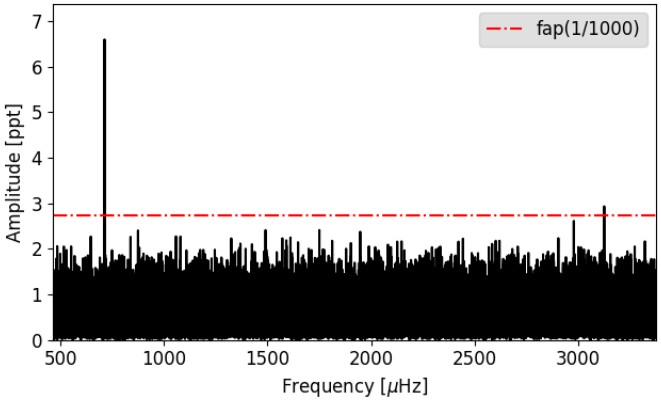

Figure 29. Fourier Transform for TIC 0114058447.

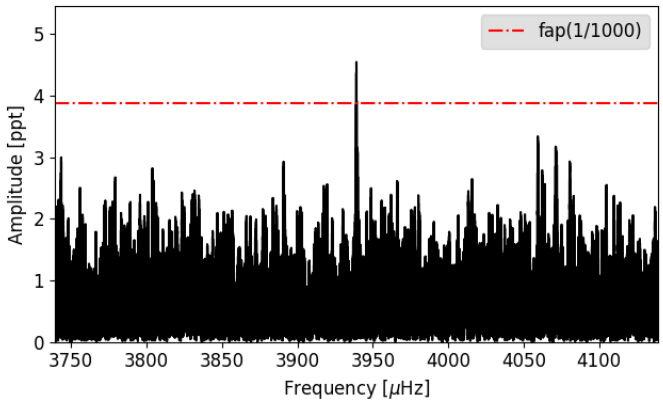

Figure 30. Fourier Transform for TIC 0141179495.

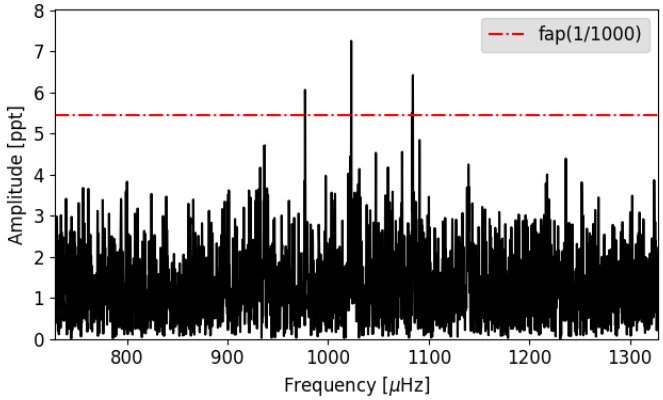

Figure 31. Fourier Transform for TIC 01159973152.

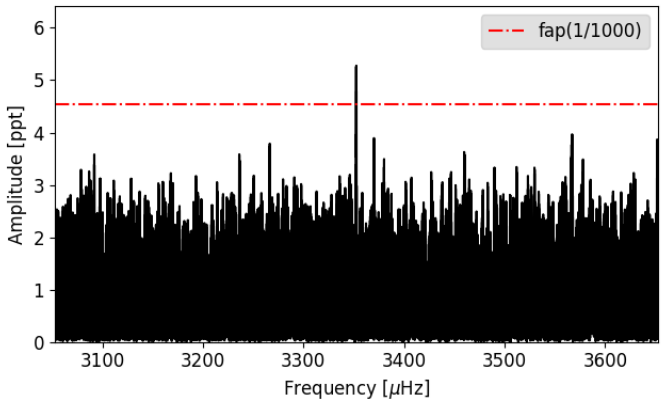

Figure 32. Fourier Transform for TIC 0192937035.

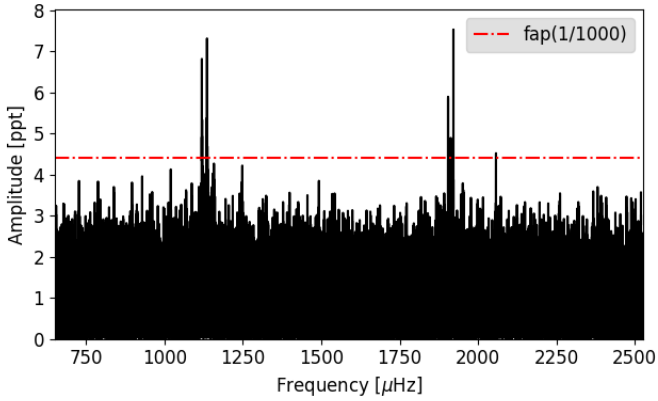

Figure 33. Fourier Transform for TIC 0201860926.

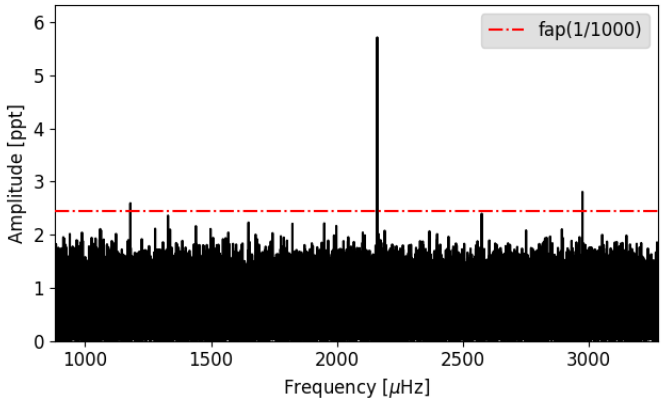

Figure 34. Fourier Transform for TIC 0264172524.

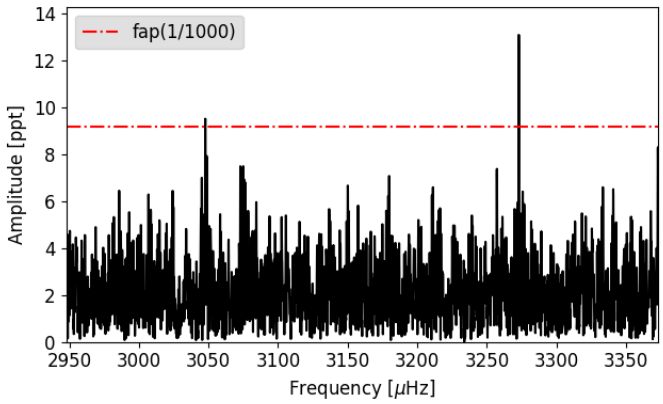

Figure 35. Fourier Transform for TIC 0375199799.

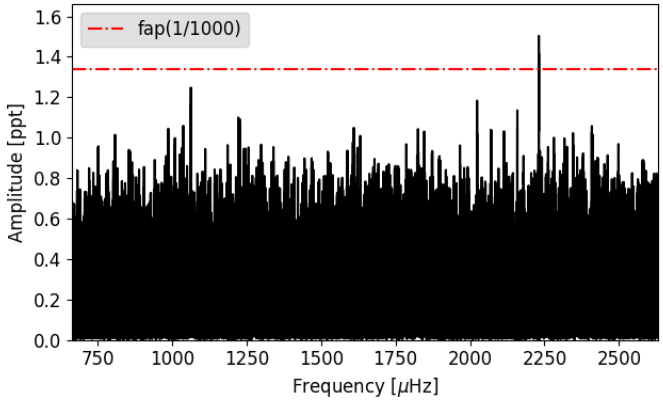

Figure 36. Fourier Transform for TIC 0409732714.

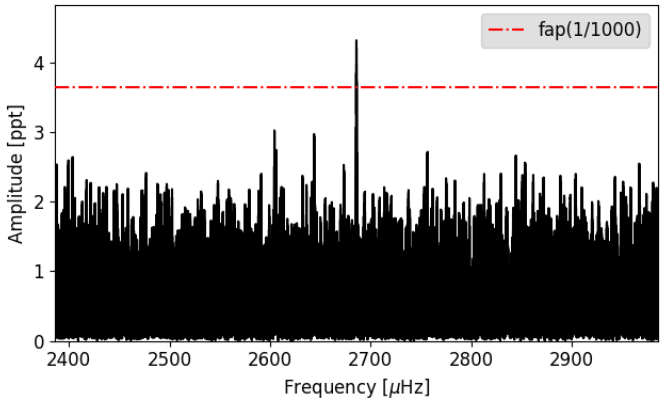

Figure 37. Fourier Transform for TIC 0423658036.

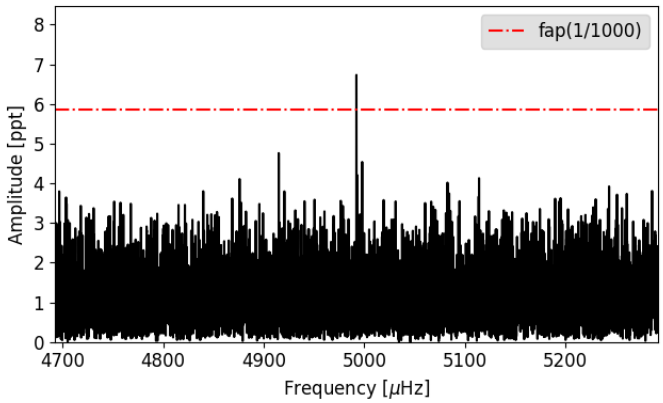

Figure 38. Fourier Transform for TIC 0453210132.

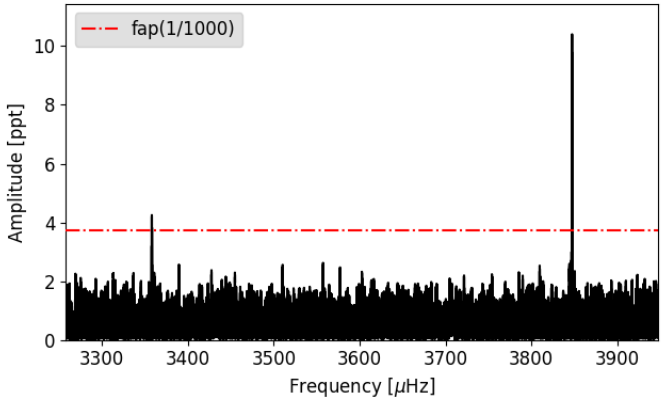

Figure 39. Fourier Transform for TIC 0461203226.

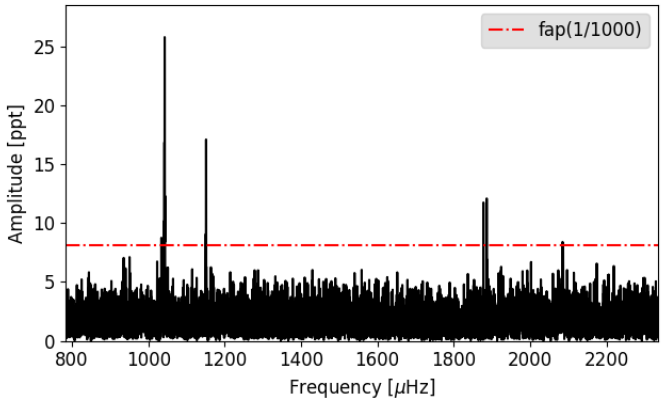

Figure 40. Fourier Transform for TIC 060589502.

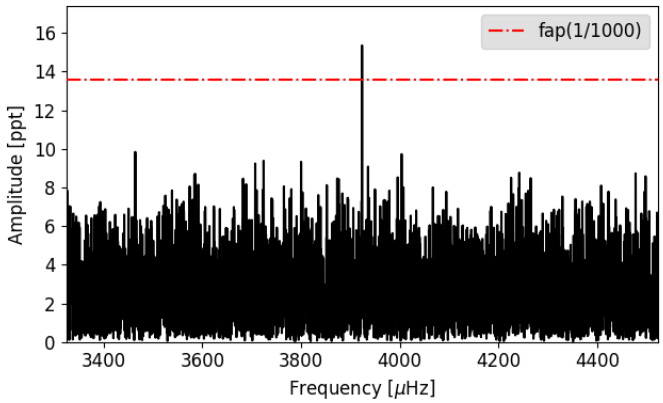

Figure 41. Fourier Transform for TIC 0640201450.

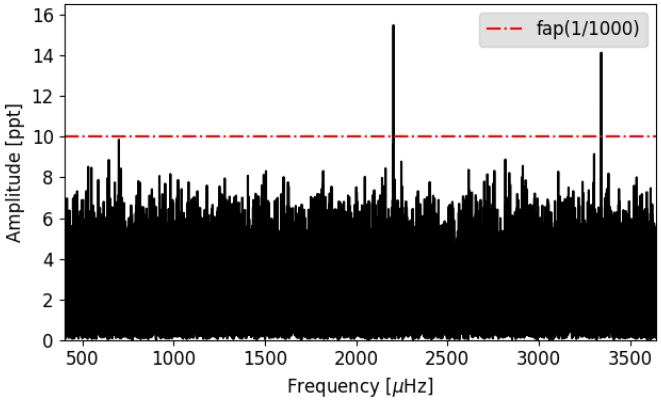

Figure 42. Fourier Transform for TIC 0762000503.

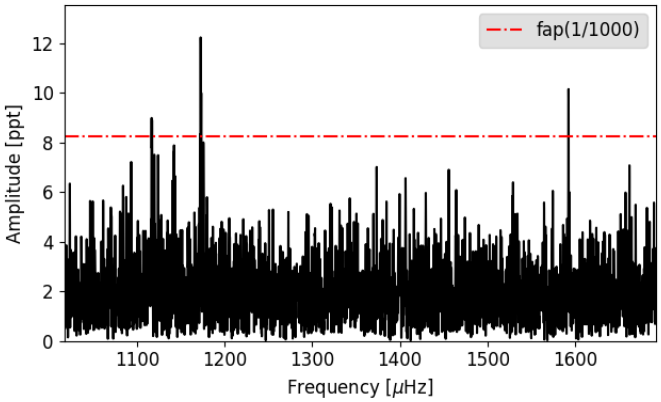

Figure 43. Fourier Transform for TIC 0775564285.

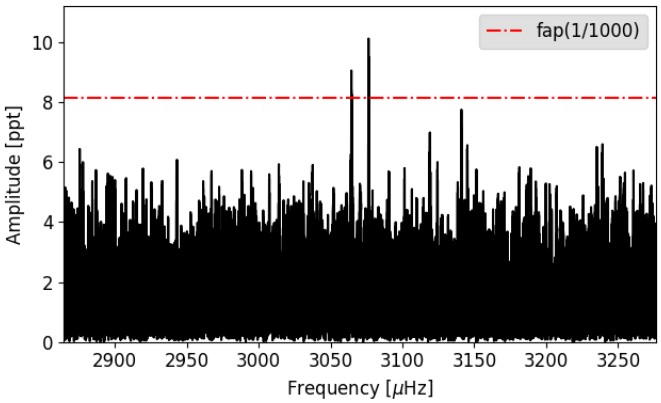

Figure 44. Fourier Transform for TIC 0800126377.

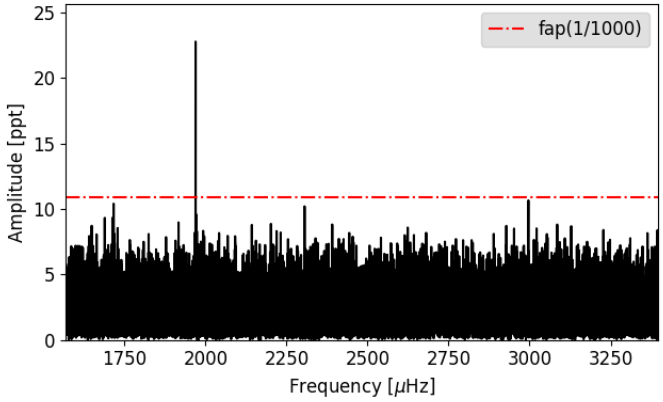

Figure 45. Fourier Transform for TIC 0800420812.

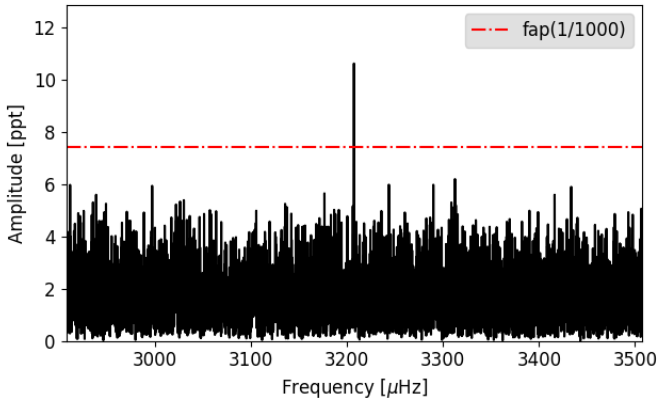

Figure 46. Fourier Transform for TIC 0842451090.

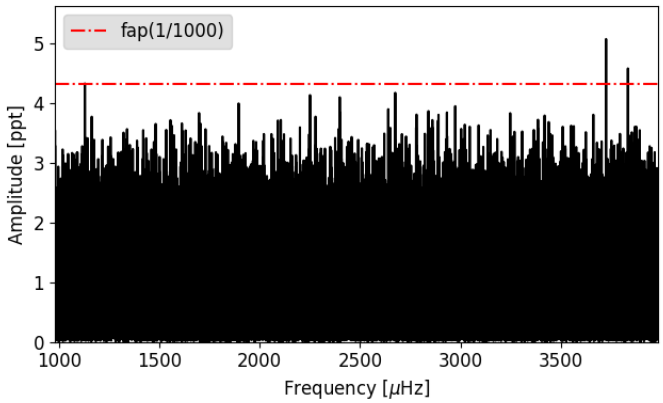

Figure 47. Fourier Transform for TIC 0900762564.

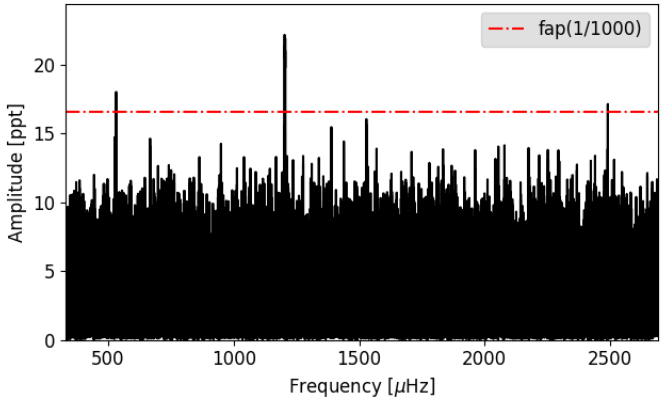

Figure 48. Fourier Transform for TIC 0902514572.

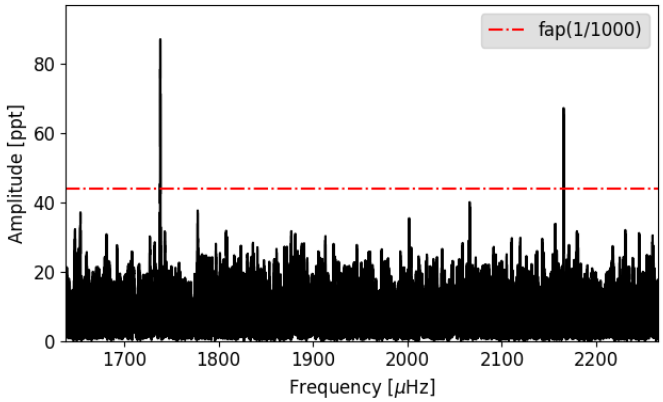

Figure 49. Fourier Transform for TIC 1860439362.

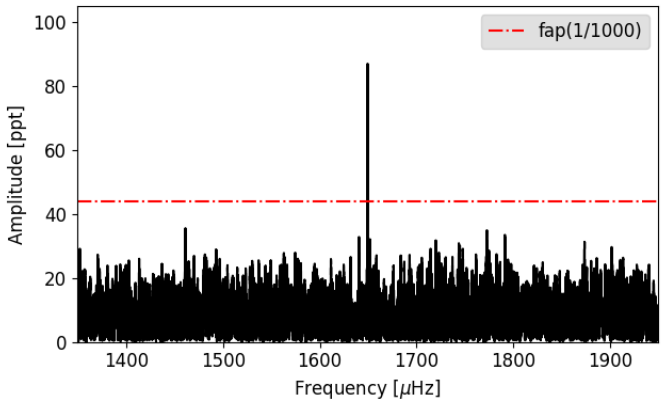

Figure 50. Fourier Transform for TIC 1944049427.

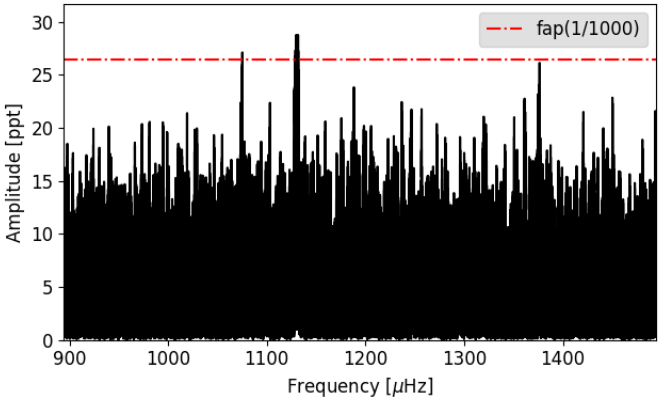

Figure 51. Fourier Transform for TIC 2045970633.